Descending Projections from the Inferior Colliculus to the Dorsal Cochlear Nucleus are Excitatory

Journal:	*Journal of Comparative Neurology*
Manuscript ID	JCN-16-0037.R2
Wiley - Manuscript type:	Research Article
Keywords:	auditory, feedback, top-down, colliculocochlear, synapses, midbrain, brainstem, AB_10013220, AB_2336337, AB_477611

Descending Projections from the Inferior Colliculus to the Dorsal Cochlear Nucleus are Excitatory

Giedre Milinkeviciute[1,2], Michael A. Muniak[1], and David K. Ryugo[1,2,3]

[1]Hearing Research, Garvan Institute of Medical Research, Sydney, NSW 2010, Australia

[2]School of Medical Sciences, Faculty of Medicine, University of New South Wales, Sydney, NSW 2052, Australia

[3]Department of Otolaryngology, Head, Neck & Skull Base Surgery, St. Vincent's Hospital, Sydney, NSW 2010, Australia

Abbreviated Title: IC Projections to DCN are Excitatory

Associate Editor: Oswald Steward, University of California-Irvine

Keywords: auditory, feedback, top-down, colliculocochlear, synapses, midbrain, brainstem, AB_477611, AB_2336337, AB_10013220

Corresponding Author: Giedre Milinkeviciute, Garvan Institute of Medical Research, 384 Victoria Street, Sydney, NSW 2010, Australia

Tel: +61 2 9295 8288

Fax: +61 2 9295 8281

Email: giedre.milin@gmail.com

Support and grant information:

UNSW APA, NHMRC 1081478 & 1080652, Oticon Foundation 15-1814, Walker Family Foundation, and gifts from Alan and Lynne Rydge and Haydn and Sue Daw.

Abstract

Ascending projections of the dorsal cochlear nucleus (DCN) primarily target the contralateral inferior colliculus (IC). In turn, the IC sends bilateral descending projections back to the DCN. We sought to determine the nature of these descending axons in order to infer circuit mechanisms of signal processing at one of the earliest stages of the central auditory pathway. An anterograde tracer was injected in the IC of CBA/Ca mice to reveal terminal characteristics of the descending axons. Retrograde tracer deposits were made in the DCN of CBA/Ca and transgenic GAD67-EGFP mice to investigate the cells giving rise to these projections. A multiunit best frequency was determined for each injection site. Brains were processed using standard histologic methods for visualization and examined by fluorescent, brightfield, and electron microscopy. Descending projections from the IC were inferred to be excitatory because the cell bodies of retrogradely labeled neurons did not co-label with EGFP expression in neurons of GAD67-EGFP mice. Furthermore, additional experiments yielded no glycinergic or cholinergic positive cells in the IC, and descending projections to the DCN co-labeled with antibodies against VGluT2, a glutamate transporter. Anterogradely labeled endings in the DCN formed asymmetric postsynaptic densities, a feature of excitatory neurotransmission. These descending projections to the DCN from the IC were topographic and suggest a feedback pathway that could underlie a frequency-specific enhancement of some acoustic signals and suppression of others. The involvement of this IC-DCN circuit is especially noteworthy when considering the gating of ascending signal streams for auditory processing.

Introduction

Hearing is an active, complex operation wherein the perception of sound requires not only detection but also attention, memory, and expectation. Underlying these processes is a rich set of interdependent brain networks that synthesize, modulate, and refine neural activity to produce a stable percept of the acoustic environment. Our working hypothesis is that the composition, design, and engineering of structures are key to revealing how the interrelated parts are assembled, which in turn informs us as to how they function together. Knowledge about how groups of neurons are interconnected can suggest computational strategies such as sequential versus parallel processing, signal amplification, feedback and/or lateral inhibition, coincidence detection, and excitatory reverberating loops. These various circuits will help define the mechanisms for the rapid discrimination of signals from noise, sharpening of sensory perceptions, and selective switching of auditory attention.

The classical view holds that incoming auditory information is processed as it ascends the auditory pathway. Acoustic signals become refined through the divergence and convergence of stimulus features that lead to fine-tuning of signals that ultimately gain significance in the auditory cortex (AC; Martin, 1994; Winer and Schreiner, 2011). In this way, auditory signals become integrated with inputs from other sensory modalities and eventually produce a percept of acoustic events embedded and represented within 3-dimensional space (Andersen et al., 1997; Driver and Spence, 1998; Budinger et al., 2006; 2008). The complexity of auditory processing becomes even more striking when one considers the presence of descending systems (reviewed in Malmierca and Ryugo, 2011). Corticofugal projections arise from throughout the AC (Diamond et al., 1969) and terminate in the medial geniculate body (MGB; Bartlett et al., 2000; Winer et al., 2001), inferior colliculus (IC; Andersen et al., 1980b; Saldana et al., 1996; Doucet

et al., 2003), and auditory brain stem (Feliciano et al., 1995; Weedman and Ryugo, 1996a,1996b; Doucet et al., 2003; Meltzer and Ryugo, 2006). The presence of corticofugal neurons is consistent with the idea of a "central processor" that modulates perception and controls behavior.

Descending projections have also been shown to arise from regions outside of the cortex—most notably the IC (Andersen et al., 1980a; Faye-Lund, 1986; Caicedo and Herbert, 1993; Malmierca et al., 1996; Thompson, 2006) and superior olivary complex (SOC; Spangler et al., 1987; Schofield, 2002). The cochlear nucleus (CN), which initiates all ascending auditory pathways, is a common target for many of these descending systems (e.g., Spangler et al., 1987; Caicedo and Herbert, 1993; Weedman and Ryugo, 1996a). The implication for these intersecting feedforward and feedback circuits is that the output signal at any station will be the collective sum of the ascending activity along with the modifications from direct and polysynaptic links from above. Feedback circuits could sharpen frequency tuning curves (Yan et al., 2005; Tang et al., 2012), calibrate directional selectivity (Zhou and Jen, 2005; Nakamoto et al., 2008), modulate response features (Ma and Suga, 2001; Yan and Ehret, 2002), or unmask acoustic signals in a noisy background (Nieder and Nieder, 1970). A better understanding of the details of these descending projections will inform us of possible mechanisms of action.

The IC has been shown to send bilateral, topographic descending projections to the dorsal cochlear nucleus (DCN; Caicedo and Herbert, 1993; Saint Marie, 1996; Malmierca et al., 1996). Many of these projections arise from the central nucleus of the IC (CNIC; Hashikawa, 1983; Faye-Lund, 1986; Schofield, 2001), providing the possibility of a direct feedback loop between the first and second synaptic stations of a major central auditory circuit. Certain details about this pathway, however, are lacking. If the projections are inhibitory in nature, they might provide lateral inhibition to sharpen frequency discrimination among the main projection

neurons of the DCN. Alternatively, the feedback could be excitatory onto inhibitory interneurons, excitatory onto excitatory projection neurons, or mixed. Furthermore, do these projections provide similar action bilaterally? In the present study, we utilized localized injections of anterograde and/or retrograde tracer dyes into the IC or DCN of mice to approach these issues.

Materials and Methods

Animals

CBA/CaH (n=8), CBA/CaJ (n=1), GAD67-EGFP (n=11), and CBGlyT2-EGFP (n=3) mice of both sexes and aged 2.5-3.5 months were used in this study. GAD67-EGFP mice express enhanced green fluorescent protein (EGFP) under the glutamic acid decarboxylase 67 (GAD67) promoter in a C57Bl/6 background and are used to label neurons containing γ-aminobutyric acid (GABA). The generation of this strain has been described elsewhere (Tamamaki et al., 2003) and animals were kindly provided by Prof. M.J. Christie (University of Sydney, Australia; Chieng et al., 2011). GlyT2-EGFP mice were generated in C57Bl/6 background and constructed to express EGFP under the promoter of the glycine transporter 2 (GlyT2) gene (Zeilhofer et al., 2005) to label glycinergic neurons and were donated by Prof. H.U. Zeilhofer (University of Zurich, Switzerland). We subsequently backcrossed GlyT2-EGFP mice onto a recipient CBA/CaH background through 10+ generations (CBGlyT2-EGFP). All procedures followed the animal care guidelines of the NHMRC and were approved by the Animal Care and Use Committee of the Johns Hopkins University School of Medicine and the Animal Ethics Committee of the Garvan Institute of Medical Research and St. Vincent's Hospital, UNSW Australia.

Surgery

Only mice with normal hearing were included in these experiments. Each animal was secured in a stereotaxic frame (Stoelting, Wood Dale, IL) with body temperature maintained at 37 °C using an infrared heating pad. Anaesthesia was maintained using isoflurane (1.5-2.0% in ~600 cc/min O_2). The top of the head was shaved and skin removed to expose the skull, which was aligned such that skull landmarks bregma and lambda were oriented horizontally along both rostrocaudal and mediolateral axes. A custom-made steel post was cemented to the skull just rostral to bregma to stabilize the animal for electrophysiological recordings (Muniak et al., 2012) and a tungsten ground-pin was inserted into the skull nearby. A small craniotomy was made directly over the target structure (DCN or IC), which was stereotaxically determined using a mouse brain atlas (Franklin and Paxinos, 2007), and subsequently covered with bone wax. The mouse was given 1 cc of saline subcutaneously for rehydration and left to recover for one day prior to electrophysiological recordings and injection.

Electrophysiology and injections

Recordings were performed in an electrically shielded, double-walled, sound attenuated chamber padded with acoustic foam (Sonora Technology Co., Gotenba, Japan). The mouse was lightly sedated with an intraperitoneal injection of acepromazine (0.07 mg/kg), restrained by placing it within a plastic tube that restricts body movement, and secured by affixing the head post to a custom-built apparatus mounted within a stereotaxic frame (David Kopf Instruments, Tujunga, CA). Bone wax was removed from the craniotomy just prior to recording.

Quartz glass micropipette electrodes filled with neuronal tracer dyes were used for multiunit recordings (inner tip diameter: 15-20 µm). For retrograde fills, a solution of cholera toxin subunit B (CTB; 0.5% in 0.05M Tris buffer, pH 7.4 and 0.15M KCl; List Biological

Laboratories, Campbell, CA) or fluoro-gold (FG; 4% in saline; Fluorochrome, Denver, CO) was used. For anterograde fills, one of three solutions of biotinylated dextran-amine (BDA; 10% in 0.05M Tris buffer, pH 7.4 and 0.15M KCl; 10,000 MW) was used: biotin (D-1956; Life Technologies, Scoresby, VIC, Australia), Mini-Emerald (ME; D-7178; Life Technologies), or Mini-Ruby (MR; D-3312; Life Technologies). In some experiments, a cocktail of both anterograde and retrograde tracers was used to simultaneously trace connections to/from the structure of interest (Coolen et al., 1999).

Stimulus delivery and neural recordings were controlled via custom software (*Batlab*; Donald Gans). Acoustic stimuli were generated digitally (DAP5016a; Microstar Laboratories, Bellevue, WA), anti-aliased (3202; Krohn-Hite, Brockton, MA), amplified (Halo A23; Parasound, San Francisco, CA), attenuated (PA5; Tucker Davis Technologies, Alachua, FL), and delivered by a calibrated free-field speaker (EMIT High Energy; Infinity, La Crescent, MN) placed 10 cm from the mouse and 25° into the sound field ipsilateral (CN) or contralateral (IC) to the hemisphere under investigation. Neural signals were amplified and filtered (2400A; Dagan, Minneapolis, MN), passed through a spike signal enhancer (40-46-1; FHC, Bowdoinham, ME), and digitized for analysis (DAP5016a; Microstar Laboratories). 200 msec broadband or sinusoidal tone search stimuli (4/sec) were delivered as the recording electrode was advanced into the brain using a motorized hydraulic micromanipulator (2650; David Kopf Instruments). Entry into the structure of interest was heralded by the presence of sound-evoked spike discharges. A frequency response area was measured using tone bursts at various intensities throughout the mouse's audible range (~4-100 kHz). From these data, the best frequency (i.e., greatest firing rate at lowest sound level) of the multiunit cluster was determined offline using *MATLAB* (MathWorks, Natick, MA). Once a suitable recording was obtained, the neuronal

tracer(s) was deposited iontophoretically using a high voltage, constant current source (CS 3; Midgard/Stoelting) set at 5 µA, 7 sec on/7 sec off for 5-10 min. The pipette was withdrawn 5 min after the termination of the injection, the craniotomy covered with bone wax, and the mouse returned to its cage. A survival period of 10-18 days ensured adequate filling of neuronal tracers (Table 2).

Tissue processing

Animals were deeply anesthetized via a lethal dose of sodium pentobarbitone, and perfused transcardially with 5 ml 1% sodium nitrite prewash in 0.1M phosphate buffered saline followed immediately by 60 ml 4% paraformaldehyde/0.1% glutaraldehyde in 0.1M phosphate buffer. Heads were postfixed overnight after which the brain was dissected from the skull, embedded in gelatin-albumin, and cut in the transverse plane at 50-60 µm using a vibrating microtome (VT1200S; Leica Systems, Nussloch, Germany). All reagents and rinses were made up in 0.12M Tris-buffered saline.

To visualize CTB labeling for fluorescent microscopy, sections were permeablized for 1 hr in 0.5% Triton X-100 (Sigma-Aldrich, St. Louis, MO), rinsed 3x, incubated for 1 hr in 1% normal rabbit serum (S-5000; Vector Laboratories, Burlingame, CA), then incubated overnight at 4 °C on a shaking platform in polyclonal goat anti-CTB primary antibody (Table 1; 1:10,000; #703, RRID:AB_10013220; List Biological Laboratories, Campbell, CA) mixed with 0.5% Triton. The next day sections were rinsed, incubated for 2 hrs in rabbit anti-goat secondary antibody conjugated with tetramethylrhodamine (1:200; A16147; Life Technologies), and rinsed again. All sections for fluorescent microscopy were mounted and coverslipped using Vectashield (H-1400; Vector Labs).

To visualize BDA/CTB labeling for brightfield and electron microscopy, sections were incubated for 10 min in 1% H_2O_2, rinsed 3x, permeabilized for 1 hour in 0.5% Photo-Flo (Kodak, Rochester, NY) or 0.5% Triton X-100 (brightfield only), and then incubated in ABC (Vectastain Elite ABC Kit, PK-6100; Vector Labs) with 0.5% Photo-Flo/Triton for 1 hr. The tissue was rinsed 3x again and BDA labeling was developed using nickel-intensified 3,3'-diaminobenzidine (DAB; Sigma-Aldrich). The tissue was rinsed and the remaining DAB was deactivated with 1% H_2O_2 for 10 min. To visualize CTB labeling, sections were blocked with 1% normal rabbit serum (Vector Labs) followed by overnight incubation at 4 °C on a shaking platform in polyclonal goat anti-CTB primary antibody (Table 1; 1:10,000; #703, RRID:AB_10013220; List Biological Labs) mixed with 0.5% Photo-Flo/Triton at 4°C. The next day, sections were rinsed and then incubated for 1 hr in biotinylated rabbit anti-goat secondary antibody (1:200; BA-5000; Vector Labs). The tissue was rinsed again, incubated in ABC with 0.5% Photo-Flo/Triton for 1 hr, rinsed, developed with DAB, and rinsed a final time. Sections for light microscopy were mounted, dehydrated, and coverslipped with Permount (Fisher Scientific, Pittsburgh, PA).

Sections selected for electron microscopy were rinsed in 0.1M maleate buffer, placed in 1% osmium tetroxide for 15 min, rinsed in maleate buffer, stained overnight in 1% uranyl acetate, dehydrated, and embedded in PolyBed 812 (Polysciences Inc., Warrington, PA) between two sheets of Aclar (Electron Microscopy Sciences, Hatfield PA). Small pieces of interest were dissected out of the polymerized PolyBed and embedded in BEEM capsules (Electron Microscopy Sciences). Serial ultrathin sections were collected in consecutive order with an ultramicrotome (PowerTome X; Boeckeler Instruments, Tucson AZ), placed on Formvar-coated

slotted grids, stained with lead citrate, and examined with an electron microscope (H7650; Hitachi, Tokyo, Japan).

To visualize immunostaining for choline acetyltransferase (ChAT) sections were incubated for 10 min in 1% H_2O_2, rinsed, and incubated for 1 hr in 0.1% Photo-Flo. The tissue was blocked for 1 hr in 10% normal goat serum (005-000-001; Jackson ImmunoResearch, West Grove, PA) and incubated overnight in monoclonal mouse anti-ChAT primary antibody (Table 1; 1:1,000; VP-C383, RRID:AB_2336337; Vector Labs) with 2% normal goat serum and 0.1% Photo-Flo at 4 °C. The next day, sections were rinsed and incubated for 1 hr in goat anti-mouse secondary antibody (1:200; BA-9200; Vector Labs), rinsed again, and then placed in ABC for another hour. Sections were rinsed and developed using nickel-intensified DAB, rinsed again, and mounted and coverslipped using Permount.

To examine the glutamatergic nature of descending collicular endings in the DCN, a deposit of ME was placed in the IC followed by immunohistochemistry for vesicular glutamate transporter 2 (VGluT2). Sections were rinsed and permeabilized with 0.25% Triton X-100 for 10 min at room temperature, blocked for 1 hr in 10% normal goat serum with 0.2% Triton, then incubated overnight in polyclonal rabbit anti-VGluT2 (Table 1; 1:1000; V-2514; RRID:AB_477611; Sigma-Aldrich) at 4 °C on a shaking platform. The next day, sections were rinsed and incubated for 1 hr in goat anti-rabbit secondary antibody conjugated with Alexa568 (1:200; A-11036; Life Technologies) at room temperature. Finally, the tissue was rinsed 3x, mounted, dehydrated, and coverslipped using Vectashield. Sections containing ME-labeled fibers with boutons in the DCN were examined at 63× with a confocal microscope (DMI6000 SP8, Leica Systems).

Tissue analysis

Standard light microscopic methods were applied to both fluorescent and brightfield images (Doucet et al., 2003; Muniak et al., 2013; Muniak and Ryugo, 2014). Images were manually enhanced using levels adjustments; as we did not quantify image intensity, such manipulations did not affect our results. Fluorescent microscopy was used to examine the locations of retrogradely labeled cells in the IC as well as potential co-labeling with EGFP. Serial section image tile sets that encompassed the entire IC were collected using a 10× objective and were automatically montaged and aligned using *TrakEM2* software (Cardona et al., 2012) with the assistance of custom Python scripts. Within *TrakEM2*, the boundary of the IC, as well as approximate subdivisions (criteria of Rockel and Jones, 1973; Faye-Lund and Osen, 1985; Loftus et al., 2008; Muniak et al., 2015), were manually traced with a graphics tablet (Cintiq 22HD; Wacom, Portland, OR), and the locations of retrogradely labeled cells in all sections of the IC were manually plotted and examined for co-labeling with EGFP using a 40× objective. Neurons located in the nucleus of the commissure were not included in this report. All values are reported as mean ± SD.

To compare cell distributions across cases, each IC was normalized along the principal axes using *MATLAB*. First, all coordinate data (e.g., cell plots, IC borders) in a given section left of the midline were reflected over the midline. Next, the maximal width (medial-lateral), height (dorsal-ventral), and length (caudal-rostral) were determined for each IC. As tissue sections were sometimes distorted within the coronal plane, the maximal width and height were computed by taking the mean size of the 5 widest (and tallest) sections. The mean maximal values across all cases were determined for all 3 dimensions, and individual cases were scaled along each dimension such that individual maxima equaled that of the global mean. This procedure ensured

that all ICs were positioned in the same bounding box while also maintaining realistic coordinate values (i.e., in μms), and facilitated the direct comparison of cell coordinate data across all cases. To quantify the central distribution of cells plotted in a given hemisphere in a given plane (e.g., coronal), normalized coordinate values were projected onto the 2D plane of interest, and the mean coordinate value (± SD) along each axis was calculated. For display purposes, an average IC outline was computed in *MATLAB* by splitting all normalized IC outlines into 20 evenly spaced bins along the rostrocaudal axis, collapsing all outlines within a given bin onto the coronal plane, determining the boundary of the region where at least 30% of these outlines overlapped, and smoothing this result.

Sections with BDA-labeled fibers and endings in the DCN were selected for EM analysis and photographed at 15,000× magnification. Micrographs containing labeled endings were visually assessed in terms of symmetry of membrane specializations in the vicinity of synapses.

Results

DCN injections and retrograde labeling in the IC

Deposits of retrograde tracer dye were made in the DCN of 14 mice (Table 2). Five animals received injections of CTB or CTB/ME (Fig. 1) and the remaining 9 animals received injections of FG or FG/MR (Figs. 2-3). CTB/ME injections were made in wild-type CBA/CaH mice (n=3); all other injections were in GAD67-EGFP transgenic mice. A multiunit best frequency was measured at each site prior to injection, with values ranging from 8 to 40 kHz (Table 2). The locus of each injection site was largely confined to the DCN with slight overlap over shared borders of the dorsal acoustic stria and posteroventral cochlear nucleus (Figs. 1-3).

Lower-frequency injections were located at progressively more ventral regions of the DCN, conforming to its known tonotopic organization (Muniak et al., 2013).

All injections resulted in bilateral retrograde labeling of cells in the IC (Figs. 1-3; Table 2). Retrograde somatic labeling from CTB injections was slightly more granular in appearance when compared to that of FG, but were otherwise similar in that both tracers resulted in partial fills of proximal dendrites. Cells matching the descriptions of both stellate and disc-shaped neurons were observed (Willard and Ryugo, 1983), but this distinction was not systematically analyzed. Total numbers of labeled cells in the IC varied from case to case, ranging from 40 to 519 (mean: 260 ± 150 cells; n=14). High cell count variability was observed for both CTB (mean: 230 ± 107 cells; n=5) and FG (mean: 277 ± 174 cells; n=9) injections. For 3 of the CTB cases, some IC sections were removed for other purposes, which likely resulted in reduced cell counts. Note, however, that one of these cases actually had the highest total count for CTB cases, further emphasizing the variability. There was no relationship between total cell counts and post-injection survival time (r^2<0.01, p=0.97; n=14). In fact, the cases with the lowest and highest counts both had the longest survival period (17 days), suggesting the variation was due to the injection itself rather than tracer degradation. We also compared total cell counts with $\log_{10}$(frequency)—which also reflects the location of the injection in the DCN (Muniak et al., 2013)—and found a modest, but not quite significant, relationship (Fig. 4A; r^2=0.28, p=0.05; n=14). This variability occurred despite efforts to maintain consistent injection parameters (e.g., tip-size, current time).

When examining the spatial distribution of retrogradely labeled cells across a series of coronal sections of the IC (Fig. 5A), we noted an apparent symmetry in the bilateral placement of cells within each hemisphere. To quantify this observation, we consolidated ipsi- and

contralateral coordinate data within a single normalized IC hemisphere (see methods) and directly compared their distributions across multiple axes in 3D (Fig. 5B-G). When projected onto either the coronal (Fig. 5B-D) or horizontal (Fig. 5E-G) plane, the central distribution of both ipsi- and contralateral cell plots occupied the same 2D region (indicated by boxes) and their spatial histograms displayed remarkably similar distributions. Furthermore, we found a clear systematic shift in the central distribution of all cell coordinates from each case with respect to $\log_{10}$(frequency) along both histogram axes of the coronal plane (dorsolateral-ventromedial: r^2=0.73, p<0.0001; dorsomedial-ventrolateral: r^2=0.69, p<0.001; n=14), as well as a minor shift along the rostro-caudal axis of the horizontal plane (r^2=0.35, p<0.05; n=14). The shifting locations of these cells were topographically related to their respective injection sites in the DCN (e.g., Fig. 3A-E), suggesting that IC neurons projecting to the DCN tend to occupy homotopic locations in the ipsi- and contralateral IC that shift with respect to their target frequency zone in the DCN.

We partitioned each IC into three main subdivisions as proposed by others (Rockel and Jones, 1973; Faye-Lund and Osen, 1985; Loftus et al., 2008; Muniak et al., 2015)—the CNIC, external cortex (ECIC) and dorsal cortex (DCIC). The ECIC was further parsed into three layers. The third layer (ECIC3) is also known as the ventrolateral nucleus (Loftus et al., 2008), and was defined in our tissue as the region of the ECIC that receives input from the lateral lemniscus and lies between the GABA 'modules' of the second layer (ECIC2) and the lateral edge of the CNIC (Figs. 1-2). This partitioning describes the different zones of the IC—CNIC, DCIC, and ECIC1, 2, 3—and was used to determine the distribution of retrogradely labeled cells in the IC. Labeled cells were identified in all subdivisions in both ipsilateral and contralateral hemispheres (Table 2). A summary of these distributions is illustrated (Fig. 4D-F) along with

individual examples of cell plots (Fig. 5) and a compilation of cells from all cases (Fig. 6). The overwhelming majority of labeled cells were located in the CNIC (ipsi mean: 78 ± 11%; contra mean: 83 ± 15%; combined mean: 79 ± 12%; Table 2) but they were also distributed in the surrounding cortices. Cases containing few cells in the ECIC or DCIC also had lower total cell counts, suggesting the absence of labeling could be attributed to incomplete tracer uptake or the location of the injection. Cells also tended to be evenly distributed between ECIC3 and the more superficial zones of ECIC1/2 (ipsi mean: 54 ± 17%; contra mean: 47 ± 15%; combined mean: 54 ± 15%; Table 2). It is possible that some identified cells were misattributed (i.e., vagary in subdivisional borders) but the vast majority of labeled cells were located well within the limits of the borders (Figs. 5-6). In particular, note the distribution of cells throughout the lateral rind, rostral pole, and medial pole of the IC. Thus, regardless of which criteria are employed for subdividing the IC, our results suggest that the DCN receives a majority of its collicular input from the CNIC.

One striking feature regarding retrogradely labeled cells was the laterality of their distribution (Fig. 4D). Labeled cells in the IC ipsilateral to the DCN injection consistently outnumbered those of the contralateral hemisphere by a factor of nearly 3 (mean ratio: 2.63 ± 0.98; n=14; Table 2). This ratio was slightly more stable with CTB injections (mean ratio: 3.02 ± 0.40; n=5) compared to FG injections (mean ratio: 2.42 ± 1.15; n=9). Only one case displayed a contralateral dominance (ratio: 0.60; Table 2, Fig. 4) but this case also had the lowest total cell count, which might reflect the size and/or location of the injection in the DCN. In the context of laterality, we also noted a conspicuous absence of retrogradely labeled cells along the far edges of the rostrolateral rind of the contralateral ECIC when viewed in the horizontal plane (Fig. 6B).

There was a significant statistical relationship between $\log_{10}$(frequency) and the ipsi/contra ratio (Fig. 4B; r^2=0.32, p=0.03; n=14), suggesting a slightly stronger ipsilateral bias for descending projections at higher frequencies. Furthermore, by restricting our analysis to those cases with full IC inclusion, this trend becomes quite robust (Fig. 4B; r^2=0.72, p<0.01; n=11). As the variability in cell counts could have contributed to this finding, we also evaluated the relationship between the ipsi/contra ratio and cell counts, and found no clear trend (Fig. 4C; r^2=0.03, p=0.59; n=14). Thus, higher frequency regions in the DCN receive a larger proportion of descending projections from the ipsilateral IC.

Co-labeling with GABAergic neurons

In order to determine the chemical nature of descending projections from the IC, injections were made in transgenic GAD67-EGFP animals (n=11). In these mice, cells that express GAD67—a rate-limiting enzyme for the synthesis of GABA—endogenously express EGFP. Examination of coronal sections throughout the IC revealed EGFP-positive neurons in all subdivisions (Figs. 1-2). However, of the 3,079 cells in either hemisphere of the IC that were labeled by injections in the DCN, not a single cell was found to co-label with EGFP expression (Figs. 1-3). This dataset included the use of two separate retrograde neural tracers. Moreover, injections were made in a number of different frequency regions of the DCN (range: 10-40 kHz), showing that the lack of co-labeling was not restricted to a particular frequency zone. Taken together, these results demonstrate that bilateral descending projections from the IC to CN are unlikely to be GABAergic.

Distribution of glycinergic neurons

Transgenic CBGlyT2-EGFP mice express EGFP under the GlyT2 promoter, resulting in the labeling of glycinergic neurons expressing GlyT2. Tissue generated from CBGlyT2-EGFP

mice (n=3) was used to document the absence of glycinergic neurons in the IC. We observed EGFP-positive neurons in the CN, lateral superior olive, and medial nucleus of the trapezoid body, as well as in other parts of the brain, which served as positive controls (Fig. 7). Although numerous EGFP-positive fibers and terminals were present in the IC, primarily in the CNIC and ECIC3, EGFP-positive somata were never observed (Fig. 7), demonstrating that the IC does not give rise to glycinergic projections.

Distribution of cholinergic neurons

We performed ChAT immunohistochemistry on a CBA/CaH mouse to test whether descending projections might be cholinergic. ChAT processing produced a brown reaction product that was evident in auditory efferent neurons distributed in the ventral nucleus of the trapezoid body and the lateral superior olive, as well as in in motoneurons of the trigeminal, abducens, and facial nuclei (Fig. 8). This positive staining of known cholinergic neurons served as positive controls for the antibody. Systematic examination of the IC revealed ChAT-positive terminals, but no ChAT-postive somata were observed (Fig. 8).

Distribution and ultrastructure of descending terminals

Unilateral deposits of the anterograde tracer, BDA, mixed with CTB were placed in the CNIC of CBA mice (n=4) in order to examine the structure of the terminal endings in the DCN bilaterally. Best frequencies at injection sites ranged from 18 to 34 kHz. Injections resulted in consistent patterns of labeling (Fig. 9). Axons from the injection site could be followed medially into the contralateral IC and ventrally into the lateral lemniscus. The ventrally directed axons descended to distribute bilaterally around the SOC and CN. Labeling in the DCN was heavier on the ipsilateral side but nonetheless topographic on both sides. Some axons terminated in the granule cell domain (GCD) and occasionally in layer I, whereas the majority formed terminal

endings bilaterally in layers II, and III of the DCN (Fig. 9). We measured the size of BDA-filled boutons from photographs taken with a brightfield microscope. Labeled terminal sizes in the DCN ranged from 0.38-18.85 μm^2 ipsilaterally (mean: 2.61 ± 1.65 μm^2; n=652) and 0.38-13.76 μm^2 contralaterally (mean 2.48 ± 1.93 μm^2; n=383).

We examined these labeled endings in the ipsilateral and contralateral DCN using an electron microscope. Endings were characterized as swellings that arose from the unmyelinated terminal portions of the axon. BDA labeled endings appeared gray-to-black from the DAB reaction product, making them readily distinguishable from unlabeled endings (Figs. 10-11). Electron-dense precipitate was present in the cytoplasm and adhered to the cytoplasmic-facing membrane surface of mitochondria, microtubules, and synaptic vesicles. Variations in the density of labeling was found in the same animal both ipsilateral and contralateral to the injection site, and was not associated with the size of the injection site in the IC or the size of the terminal in the DCN (Figs. 10-11).

It is generally accepted that the shape of synaptic vesicles (Uchizono, 1965) and/or the symmetry of pre- and postsynaptic membrane thickenings around the release site (Gray, 1959) are related to the excitatory or inhibitory action at the synapse. Labeled terminal swellings were filled with synaptic vesicles but the DAB reaction product partially obscured the vesicular membrane, making accurate measurements of synaptic vesicles impossible (Fig. 10). Synapses were identified by an accumulation of synaptic vesicles around short stretches of opposing pre- and postsynaptic membrane thickenings, referred to as postsynaptic densities (PSDs). In every case examined, labeled endings formed asymmetric PSDs where the postsynaptic thickening was more prominent than the presynaptic thickening (Fig. 11). Thus, the morphology of the membrane specializations was consistent with excitatory action.

Co-labeling with VGlut2 puncta

Immunohistochemical characterization of descending collicular terminals utilized a unilateral ME injection in the CNIC of a CBA/CaH mouse (n=1). As with BDA tissue (above), labeled collicular axons and terminals were observed in the DCN bilaterally with an ipsilateral predominance. Sections containing the DCN were immunostained with antibodies raised against VGluT2 and an Alexa568 secondary, and were examined with a confocal microscope. Descending boutons labeled with ME consistently co-labeled with VGlut2 puncta as seen in three dimensions (Fig. 12). These observations supported the case for the glutamatergic, excitatory nature of descending projections from the IC to the DCN.

Discussion

Previous reports have established that the IC sends bilateral and topographic descending projections to the DCN in various species, including the cat (Hashikawa, 1983), rat (Faye-Lund, 1986; Caicedo and Herbert, 1993; Malmierca et al., 1996), chinchilla (Saint Marie, 1996), and guinea pig (Ostapoff et al., 1990; Malmierca et al., 1996; Schofield, 2001). The current results demonstrate a similar projection in the mouse. In addition, our observations extend previous findings by quantifying a large ipsilateral predisposition to this projection that includes an increasing bias at higher frequencies. Moreover, we showed that these axons originate from IC neurons whose terminals exhibit the characteristics of excitatory synapses. The details of this feedback input establish parameters that constrain the range of possible mechanisms involved in how the IC might modulate ascending signals from the DCN.

Distribution of IC neurons projecting to the DCN

Anatomical variation is part of the process of speciation. Thus, a map of subdivisions for the IC of one species is not necessarily identical to that of another. Moreover, different researchers often use different methods, descriptive criteria, and terminology for different species (e.g., Ramón y Cajal, 1911; Morest and Oliver, 1984; Oliver and Morest, 1984; Faye-Lund and Osen, 1985; Meininger et al., 1986). We used the basic subdivisions for which there is general agreement: central nucleus, dorsal cortex, and external cortex. We prefer the term external cortex (as opposed to lateral cortex) because this lateral region in the mouse extends ventrally and rostrally. We distinguished the third, deepest layer of the external cortex (ECIC3; the ventrolateral nucleus of Loftus et al., 2008) by virtue of its topographic input from the lateral lemniscus (Muniak et al., 2015). ECIC2 was characterized by the presence of GABA modules, featuring GABA-positive cell bodies clustered into narrow islands and sandwiched between ECIC3 and ECIC1, which is the superficial layer composed of mostly fibers.

Previous reports have described the locations of neurons projecting to the DCN from the IC (Kane and Finn, 1977; Hashikawa and Kawamura, 1983; Hashikawa, 1983; Faye-Lund, 1986; Okoyama et al., 2006; Ostapoff et al., 1990; Schofield, 2001), but the relative contributions from each subdivision have not been quantified. Furthermore, qualitative descriptions are in conflict with one another—in cat, the CNIC is reported to be the largest contributor to descending projections (Hashikawa, 1983), whereas in rat, the projecting cells are found primarily in the ECIC (Faye-Lund, 1986). Note however, that in this latter study (Faye-Lund, 1986) a majority of these cells were located within the deep layer (ECIC3), suggesting that despite this regional disparity, projecting cells tended to originate from areas receiving lateral lemniscal input. The present results suggest that, in mouse, the IC sends projections from all three major subdivisions,

with the largest contribution arising from the CNIC (CNIC:ECIC3:ECIC1/2:DCIC ratio: 1.00:0.10:0.10:0.08). Nonetheless, our composite 3D plot of the distribution of labeled cells (Fig. 6) provides clear evidence that: 1) projecting cells reside in all corners of the IC, thereby implicating non-lemniscal subdivisions to some degree, and 2) the greatest density of labeled neurons is located in the central core of the IC, equivalent to the CNIC. Disparities with other reports (Hashikawa, 1983; Faye-Lund, 1986) could be due to differences in retrograde tracer sensitivity, methods for subdividing the IC, detection threshold sensitivity, and/or species differences. It is worth noting that our study utilized focal deposits of tracer restricted to the DCN. Previous reports, particularly those that qualified subdivision differences, utilized larger tracer deposits that encompassed the majority of the CN, which may result in skewed distributions relative to our DCN-based counts.

Our results suggest that cells of the IC giving rise to descending projections to the DCN are distributed in symmetric locations across the ipsi- and contralateral hemispheres. Furthermore, we observed shifts in this distribution when the DCN injection site varied with respect to best frequency, with the direction of this shift conforming to the approximate tonotopic gradient of the IC (Clopton et al., 1974; Portfors et al., 2011). Thus, it would appear that much of the descending projection operates in a topographic and frequency specific manner. In addition, the two hemispheres of the IC are heavily interconnected via commissural fibers (Saldana and Merchan, 1992; Malmierca et al., 2009), facilitating the frequency-specific exchange of information (Malmierca et al., 2005). It is therefore possible that descending neurons of the IC may also be connected via commissural projections. Such connectivity could allow for the integration of binaural information prior to sending signals back to the DCN.

While the DCN receives input from both IC hemispheres, only a few studies have commented on the laterality of this projection. A slight ipsilateral predominance has been described in cat (Hashikawa, 1983), with a stronger ipsilateral bias quantified in guinea pig (median ipsi/contra ratio: 1.8; n=6; Schofield, 2001) and rat (mean ipsi/contra ratio: 1.6; n=4; CNIC only; Okoyama et al., 2006). Our results show an even more robust ipsilateral bias in the mouse (mean ratio: 2.63 ± 0.98; n=14) independent of the frequency zone of the DCN where the tracer was deposited. As with intra-hemispheric counts, the fact that our injections were restricted to the DCN might explain the larger ratio value—earlier studies could not disambiguate between IC neurons that specifically target the DCN, the VCN, or the GCD. Nonetheless, all studies are in agreement that there is some degree of ipsilateral dominance to the descending projection from the IC. By making small deposits in different frequency zones of the DCN, we demonstrate that this bias is a modular phenomenon that exists throughout the nucleus and that it favors high frequency projections. Given that this ipsilateral projection is most likely activated by sounds in the contralateral hemisphere, it may supply the DCN with information regarding sounds highly lateralized to the opposite hemisphere. However, in consideration of commissural connectivity, it is also possible that ispilateral-descending neurons may in fact be modulated or under the direct control of the contralateral IC, thereby resulting in a more "balanced" descending influence from the IC.

This ipsilateral descending bias for higher frequencies merits a comment in the context of sound localization. Spectral notches of head-related transfer functions in the mouse are found at frequencies above 20 kHz (Lauer et al., 2011). As the DCN-CNIC circuit plays a crucial role in processing spectral cues critical for localization in the vertical plane (Young et al., 1992; May, 2000; Davis et al., 2003), a stronger ipsilateral descending projection in this higher frequency

range could function to provide contralateral context to the spectral cue computations in the DCN. Further investigations will be required to explore the presence of this frequency bias in its role for sound processing.

Characterization of IC neurons projecting to the DCN

We used neurotransmitter profiles of cells to identify different neuronal subtypes and establish which types of cells project to the DCN. Designing circuit mechanisms for how these connections might function will depend on their excitatory or inhibitory action. While the IC receives glycinergic (present results; Sanes et al., 1987; Pourcho et al., 1992; Vater et al., 1992b), serotonergic (Obara et al., 2014), dopaminergic (Nevue et al., 2016) and cholinergic (Schofield, 2010; Ayala and Malmierca, 2015) inputs, these neurotransmitters are not found in IC somata (Benson and Potashner, 1990; Pourcho et al., 1992; Merchan et al., 2005; Nevue et al., 2016). These results are consistent with our ChAT-stained CBA/CaH mice and CBGlyT2-EGFP transgenic mice where neither ChAT-positive nor glycinergic somata were observed anywhere in the IC. Thus, descending projections arising from the IC are not cholinergic or glycinergic.

GABA-positive neurons have been found in the IC of the rat (Roberts and Ribak, 1987), bat (Vater et al., 1992a), cat (Winer et al., 1996), gerbil (Gleich et al., 2014), guinea pig (Foster et al., 2014), and mouse (Ono et al., 2005), where they comprise roughly 20-25% of both stellate and disc-shaped neurons (cat: Oliver et al., 1994; bat: Winer et al., 1995; rat: Merchan et al., 2005). Our co-labeling results in GAD67-EGFP mice demonstrate that GABAergic neurons in the IC do not send descending projections to the DCN in the mouse, suggesting that they are excitatory, a conclusion consistent with what has been reported for guinea pig (Ostapoff et al., 1990). Furthermore, the majority of glutamatergic neurons in the IC express VGluT2 (Ito et al.,

2011; Hackett et al., 2011; Ito et al., 2015) and we showed that IC projections to the DCN are VGluT2-positive and thus likely excitatory in nature.

Ultrastructural characteristics of collicular endings in the DCN

Labeled terminals from the IC were distributed across the layers of the DCN (Caicedo and Herbert, 1993; Malmierca et al., 1996), although terminals in layer I were sparse. At the ultrastructural level, the symmetry of PSDs formed by labeled descending boutons were used to infer mode of action. PSDs are not always evident in ultrathin sections but when present, were used to indicate excitatory or inhibitory synaptic transmission. Thus, whenever possible we used the relative symmetry of PSDs as a criterion to determine synapse type (Uchizono, 1965; Tisdale and Nakajima, 1976). Labeled endings in our study exhibited asymmetric PSDs with their targets, supporting our conclusion that projections from the IC to the DCN have an excitatory action.

Targets of collicular projections to the DCN

Interpretation of the action of the feedback projection between the IC and DCN requires knowledge not only about the originating neuron type but that of its target cell as well. Given that descending projections from the IC appear to be excitatory and topographic, they must exert their influence through the frequency-specific activation of target neurons, such as pyramidal neurons, the primary projection neurons of the DCN. These cells occupy layer II of the DCN (Ramón y Cajal, 1909; Brawer et al., 1974; Lorente de Nó, 1981; Blackstad et al., 1984), where we observed the densest BDA labeling. Frequency-specific targeting of pyramidal cells would amplify signals they receive from the AN. Additionally, BDA staining was present in layer III where giant cells, the other DCN projection neuron, are situated (Ryugo and Willard, 1985). Predicting what effect feedback excitation would have on these neurons is more difficult because

their function has not been established (Cant and Benson, 2003). Together, these excitatory descending projections could be driving excitatory neurons to establish a localized reverberatory loop that amplifies the signal or more simply raises the excitability index of the resident neurons.

A feedback excitation pathway from the IC may also target inhibitory cells of the DCN that participate in feedforward inhibition of pyramidal cells (Cant and Benson, 2003). This arrangement might serve to suppress the transmission of incoming AN signals. Inhibitory neurons might also take part in lateral inhibition to silence neurons with adjacent frequency sensitivities, thereby sharpening frequency boundaries and enhancing particular signals.

Other excitatory neurons in the DCN may also be targets of descending projections from the IC. Granule cells integrate multimodal information (Wright and Ryugo, 1996; Shore et al., 2000; Ohlrogge et al., 2001; Ryugo et al., 2003; Haenggeli et al., 2005; Zhan et al., 2006; Zhan and Ryugo, 2007), and may be the recipient of labeled terminals observed in the GCD as well as throughout the neuropil of the DCN. Granule cells regulate pyramidal cell firing by direct excitatory input (Blackstad et al., 1984; Davis and Young, 1997; Rubio et al., 2008) or indirect inhibition via cartwheel cells after combining non-auditory information with auditory inputs (Manis et al., 1994). If parallel fibers of granule cells make synaptic contact with cartwheel interneurons, the end result is feed-forward inhibition.

Somatosensory integration is particularly relevant in the context of head and pinna position, where proprioceptive afferents from periauricular skin and muscle influence DCN output via granule cell pathways (Rice et al., 1992, 1995; Kanold and Young, 2001). Knowledge of head and pinna position is crucial for the accurate localization of sounds in space, and top-down modulation of this circuit could be a means to improve accuracy. This type of circuit could possibly help localize an elevated sound (Masterson and Diamond, 1967) or boost our

attention to the sound source through pooling different sensory inputs (Weedman and Ryugo, 1996a; Wright and Ryugo, 1996; Ohlrogge et al., 2001; Haenggeli et al., 2005; Zhan et al., 2006; Zhan and Ryugo, 2007). Additionally, it has been suggested that DCN circuitry resembles that of the cerebellum (Oertel and Young, 2004) and could be involved in dampening self-generated, expected, or continuous sounds (Requarth and Sawtell, 2011). The wide range of multimodal inputs that converge upon the IC, together with individual neuronal functional characteristics, conceivably help to construct a coherent acoustic scene and selectively gate behaviorally important sounds. Therefore, information relayed from various subdivisions of the IC to the DCN may be one way for the auditory system to focus on the most relevant signals within incoming acoustic streams.

Other acknowledgements

The authors would like to acknowledge the technical assistance provided by Katanyu Pongstaporn for immunohistochemical and electron microscopic processing, Catherine Connelly for sharing ChAT-stained tissue, and the reviewers for their constructive comments on the manuscript.

Conflict of interest statement

The authors declare no conflict of interest.

Role of authors

The authors had full access to all the data in the study and take responsibility for the integrity of the data and accuracy of the analysis. Study concept and design: GM, MAM, and DKR. Acquisition of Data: GM. Analysis and interpretation of data: GM, MAM, and DKR. Drafting and revising the manuscript: GM, MAM, and DKR. Obtained Funding: APA UNSW Australia, GM; grants and lab donations, DKR.

Literature cited

Andersen RA, Roth GL, Aitkin LM, Merzenich MM. 1980a. The efferent projections of the central nucleus and the pericentral nucleus of the inferior colliculus in the cat. J Comp Neurol 194(3):649-662.

Andersen RA, Snyder LH, Bradley DC, Xing J. 1997. Multimodal representation of space in the posterior parietal cortex and its use in planning movements. Annu Rev Neurosci 20:303-330.

Andersen RA, Snyder RL, Merzenich MM. 1980b. The topographic organization of corticocollicular projections from physiologically identified loci in the AI, AII, and anterior auditory cortical fields of the cat. J Comp Neurol 191(3):479-494.

Ayala YA, Malmierca MS. 2015. Cholinergic Modulation of Stimulus-Specific Adaptation in the Inferior Colliculus. J Neurosci 35(35):12261-12272.

Bartlett EL, Stark JM, Guillery RW, Smith PH. 2000. Comparison of the fine structure of cortical and collicular terminals in the rat medial geniculate body. Neuroscience 100(4):811-828.

613 Benson CG, Potashner SJ. 1990. Retrograde transport of [3H]glycine from the cochlear nucleus
614 to the superior olive in the guinea pig. J Comp Neurol 296(3):415-426.
615 Blackstad TW, Osen KK, Mugnaini E. 1984. Pyramidal neurones of the dorsal cochlear nucleus:
616 a Golgi and computer reconstruction study in cat. Neuroscience 13(3):827-854.
617 Brawer JR, Morest DK, Kane EC. 1974. The neuronal architecture of the cochlear nucleus of the
618 cat. J Comp Neurol 155(3):251-300.
619 Budinger E, Heil P, Hess A, Scheich H. 2006. Multisensory processing via early cortical stages:
620 Connections of the primary auditory cortical field with other sensory systems.
621 Neuroscience 143(4):1065-1083.
622 Budinger E, Laszcz A, Lison H, Scheich H, Ohl FW. 2008. Non-sensory cortical and subcortical
623 connections of the primary auditory cortex in Mongolian gerbils: bottom-up and top-
624 down processing of neuronal information via field AI. Brain Res 1220:2-32.
625 Caicedo A, Herbert H. 1993. Topography of descending projections from the inferior colliculus
626 to auditory brainstem nuclei in the rat. J Comp Neurol 328(3):377-392.
627 Cant NB, Benson CG. 2003. Parallel auditory pathways: projection patterns of the different
628 neuronal populations in the dorsal and ventral cochlear nuclei. Brain Res Bull 60(5-
629 6):457-474.
630 Cardona A, Saalfeld S, Schindelin J, Arganda-Carreras I, Preibisch S, Longair M, Tomancak P,
631 Hartenstein V, Douglas RJ. 2012. TrakEM2 software for neural circuit reconstruction.
632 PLoS One 7(6):e38011.
633 Chieng B, Azriel Y, Mohammadi S, Christie MJ. 2011. Distinct cellular properties of identified
634 dopaminergic and GABAergic neurons in the mouse ventral tegmental area. J Physiol
635 589(Pt 15):3775-3787.

636 Clopton BM, Winfield JA, Flammino FJ. 1974. Tonotopic organization: review and analysis.
637 Brain Res 76(1):1-20.
638 Coolen LM, Jansen HT, Goodman RL, Wood RI, Lehman MN. 1999. A new method for
639 simultaneous demonstration of anterograde and retrograde connections in the brain: co-
640 injections of biotinylated dextran amine and the beta subunit of cholera toxin. J Neurosci
641 Methods 91(1-2):1-8.
642 Davis KA, Ramachandran R, May BJ. 2003. Auditory processing of spectral cues for sound
643 localization in the inferior colliculus. J Assoc Res Otolaryngol 4(2):148-163.
644 Davis KA, Young ED. 1997. Granule cell activation of complex-spiking neurons in dorsal
645 cochlear nucleus. J Neurosci 17(17):6798-6806.
646 Diamond IT, Jones EG, Powell TP. 1969. The projection of the auditory cortex upon the
647 diencephalon and brain stem in the cat. Brain Res 15(2):305-340.
648 Doucet JR, Molavi DL, Ryugo DK. 2003. The source of corticocollicular and corticobulbar
649 projections in area Te1 of the rat. Exp Brain Res 153(4):461-466.
650 Driver J, Spence C. 1998. Attention and the crossmodal construction of space. Trends Cogn Sci
651 2(7):254-262.
652 Faye-Lund H. 1986. Projection from the inferior colliculus to the superior olivary complex in the
653 albino rat. Anat Embryol (Berl) 175(1):35-52.
654 Faye-Lund H, Osen KK. 1985. Anatomy of the inferior colliculus in rat. Anat Embryol (Berl)
655 171(1):1-20.
656 Feliciano M, Saldaña E, Mugnaini E. 1995. Direct projections from the rat primary auditory
657 neocortex to nucleus sagulum, paralemniscal regions, superior olivary complex and
658 cochlear nuclei. Auditory Neuroscience 1:287-308.

659 Foster NL, Mellott JG, Schofield BR. 2014. Perineuronal nets and GABAergic cells in the
660 inferior colliculus of guinea pigs. Front Neuroanat 7:53.
661 Franklin KBJ, Paxinos G. 2007. The Mouse Brain in Stereotaxic Coordinates. San Diego, CA:
662 Academic Press.
663 Gleich O, Netz J, Strutz J. 2014. Comparing the inferior colliculus of young and old gerbils
664 (Meriones unguiculatus) with an emphasis on GABA. Exp Gerontol 57:155-162.
665 Gray EG. 1959. Axo-somatic and axo-dendritic synapses of the cerebral cortex: an electron
666 microscope study. J Anat 93:420-433.
667 Hackett TA, Takahata T, Balaram P. 2011. VGLUT1 and VGLUT2 mRNA expression in the
668 primate auditory pathway. Hear Res 274(1-2):129-141.
669 Haenggeli CA, Pongstaporn T, Doucet JR, Ryugo DK. 2005. Projections from the spinal
670 trigeminal nucleus to the cochlear nucleus in the rat. J Comp Neurol 484(2):191-205.
671 Hashikawa T. 1983. The inferior colliculopontine neurons of the cat in relation to other collicular
672 descending neurons. J Comp Neurol 219(2):241-249.
673 Hashikawa T, Kawamura K. 1983. Retrograde labeling of ascending and descending neurons in
674 the inferior colliculus. A fluorescent double labelling study in the cat. Exp Brain Res
675 49(3):457-461.
676 Ito T, Bishop DC, Oliver DL. 2011. Expression of glutamate and inhibitory amino acid vesicular
677 transporters in the rodent auditory brainstem. J Comp Neurol 519(2):316-340.
678 Ito T, Inoue K, Takada M. 2015. Distribution of glutamatergic, GABAergic, and glycinergic
679 neurons in the auditory pathways of macaque monkeys. Neuroscience 310:128-151.
680 Kane ES, Finn RC. 1977. Descending and intrinsic inputs to dorsal cochlear nucleus of cats: a
681 horseradish peroxidase study. Neuroscience 2(6):897-912.

682 Kanold PO, Young ED. 2001. Proprioceptive information from the pinna provides
683 somatosensory input to cat dorsal cochlear nucleus. J Neurosci 21(19):7848-7858.
684 Lauer AM, Slee SJ, May BJ. 2011. Acoustic basis of directional acuity in laboratory mice. J
685 Assoc Res Otolaryngol 12(5):633-645.
686 Loftus WC, Malmierca MS, Bishop DC, Oliver DL. 2008. The cytoarchitecture of the inferior
687 colliculus revisited: a common organization of the lateral cortex in rat and cat.
688 Neuroscience 154(1):196-205.
689 Lorente de Nó R. 1981. The Primary Acoustic Nuclei. New York: Raven Press.
690 Ma X, Suga N. 2001. Corticofugal modulation of duration-tuned neurons in the midbrain
691 auditory nucleus in bats. Proc Natl Acad Sci U S A 98(24):14060-14065.
692 Malmierca MS, Hernandez O, Antunes FM, Rees A. 2009. Divergent and point-to-point
693 connections in the commissural pathway between the inferior colliculi. J Comp Neurol
694 514(3):226-239.
695 Malmierca MS, Hernandez O, Rees A. 2005. Intercollicular commissural projections modulate
696 neuronal responses in the inferior colliculus. Eur J Neurosci 21(10):2701-2710.
697 Malmierca MS, Le Beau FE, Rees A. 1996. The topographical organization of descending
698 projections from the central nucleus of the inferior colliculus in guinea pig. Hear Res
699 93(1-2):167-180.
700 Malmierca MS, Ryugo DK. 2011. Descending Connections of Auditory Cortex to the Midbrain
701 and Brain Stem. In: Winer JA, Schreiner CE, editors. The Auditory Cortex. New York:
702 Springer. p 189-208.

703 Manis PB, Spirou GA, Wright DD, Paydar S, Ryugo DK. 1994. Physiology and morphology of
704 complex spiking neurons in the guinea pig dorsal cochlear nucleus. J Comp Neurol
705 348(2):261-276.
706 Martin KA. 1994. A brief history of the "feature detector". Cereb Cortex 4(1):1-7.
707 Masterson B, Diamond IT. 1967. Medial superior olive and sound localization. Science
708 155(3770):1696-1697.
709 May BJ. 2000. Role of the dorsal cochlear nucleus in the sound localization behavior of cats.
710 Hear Res 148(1-2):74-87.
711 Meininger V, Pol D, Derer P. 1986. The inferior colliculus of the mouse. A Nissl and Golgi
712 study. Neuroscience 17(4):1159-1179.
713 Meltzer NE, Ryugo DK. 2006. Projections from auditory cortex to cochlear nucleus: A
714 comparative analysis of rat and mouse. Anat Rec A Discov Mol Cell Evol Biol
715 288(4):397-408.
716 Merchan M, Aguilar LA, Lopez-Poveda EA, Malmierca MS. 2005. The inferior colliculus of the
717 rat: quantitative immunocytochemical study of GABA and glycine. Neuroscience
718 136(3):907-925.
719 Morest DK, Oliver DL. 1984. The neuronal architecture of the inferior colliculus in the cat:
720 defining the functional anatomy of the auditory midbrain. J Comp Neurol 222(2):209-
721 236.
722 Muniak MA, Mayko ZM, Ryugo DK, Portfors CV. 2012. Preparation of an awake mouse for
723 recording neural responses and injecting tracers. J Vis Exp(64).

Muniak MA, Milinkeviciute G, Ryugo DK. 2015. 3D Model of Frequency Representation in the Inferior Colliculus of the CBA/Ca Mouse. Proceedings of the Association for Research in Otolaryngology (abstract 559); Baltimore, MD.

Muniak MA, Rivas A, Montey KL, May BJ, Francis HW, Ryugo DK. 2013. 3D model of frequency representation in the cochlear nucleus of the CBA/J mouse. J Comp Neurol 521(7):1510-1532.

Muniak MA, Ryugo DK. 2014. Tonotopic organization of vertical cells in the dorsal cochlear nucleus of the CBA/J mouse. J Comp Neurol 522(4):937-949.

Nakamoto KT, Jones SJ, Palmer AR. 2008. Descending projections from auditory cortex modulate sensitivity in the midbrain to cues for spatial position. J Neurophysiol 99(5):2347-2356.

Nevue AA, Elde CJ, Perkel DJ, Portfors CV. 2016. Dopaminergic Input to the Inferior Colliculus in Mice. Front Neuroanat 9:168.

Nieder P, Nieder I. 1970. Antimasking effect of crossed olivocochlear bundle stimulation with loud clicks in guinea pig. Exp Neurol 28(1):179-188.

Obara N, Kamiya H, Fukuda S. 2014. Serotonergic modulation of inhibitory synaptic transmission in mouse inferior colliculus. Biomed Res 35(1):81-84.

Oertel D, Young ED. 2004. What's a cerebellar circuit doing in the auditory system? Trends Neurosci 27(2):104-110.

Ohlrogge M, Doucet JR, Ryugo DK. 2001. Projections of the pontine nuclei to the cochlear nucleus in rats. J Comp Neurol 436(3):290-303.

Okoyama S, Ohbayashi M, Ito M, Harada S. 2006. Neuronal organization of the rat inferior colliculus participating in four major auditory pathways. Hear Res 218(1-2):72-80.

747 Oliver DL, Morest DK. 1984. The central nucleus of the inferior colliculus in the cat. J Comp
748 Neurol 222(2):237-264.
749 Oliver DL, Winer JA, Beckius GE, Saint Marie RL. 1994. Morphology of GABAergic neurons
750 in the inferior colliculus of the cat. J Comp Neurol 340(1):27-42.
751 Ono M, Yanagawa Y, Koyano K. 2005. GABAergic neurons in inferior colliculus of the
752 GAD67-GFP knock-in mouse: electrophysiological and morphological properties.
753 Neurosci Res 51(4):475-492.
754 Ostapoff EM, Morest DK, Potashner SJ. 1990. Uptake and retrograde transport of [3H]GABA
755 from the cochlear nucleus to the superior olive in the guinea pig. J Chem Neuroanat
756 3(4):285-295.
757 Portfors CV, Mayko ZM, Jonson K, Cha GF, Roberts PD. 2011. Spatial organization of receptive
758 fields in the auditory midbrain of awake mouse. Neuroscience 193:429-439.
759 Pourcho RG, Goebel DJ, Jojich L, Hazlett JC. 1992. Immunocytochemical evidence for the
760 involvement of glycine in sensory centers of the rat brain. Neuroscience 46(3):643-656.
761 Ramón y Cajal S. 1909. Histologie du Système Nerveux de l'Homme et des Vertébrés. Paris:
762 Maloine.
763 Ramón y Cajal S. 1911. Histologie du Système Nerveux de l'Homme et des Vertébrés. Paris:
764 Maloine.
765 Requarth T, Sawtell NB. 2011. Neural mechanisms for filtering self-generated sensory signals in
766 cerebellum-like circuits. Curr Opin Neurobiol 21(4):602-608.
767 Rice JJ, May BJ, Spirou GA, Young ED. 1992. Pinna-based spectral cues for sound localization
768 in cat. Hear Res 58(2):132-152.

769 Rice JJ, Young ED, Spirou GA. 1995. Auditory-nerve encoding of pinna-based spectral cues:
770 rate representation of high-frequency stimuli. J Acoust Soc Am 97(3):1764-1776.
771 Roberts RC, Ribak CE. 1987. An electron microscopic study of GABAergic neurons and
772 terminals in the central nucleus of the inferior colliculus of the rat. J Neurocytol
773 16(3):333-345.
774 Rockel AJ, Jones EG. 1973. The neuronal organization of the inferior colliculus of the adult cat.
775 II. The pericentral nucleus. J Comp Neurol 149(3):301-334.
776 Rubio ME, Gudsnuk KA, Smith Y, Ryugo DK. 2008. Revealing the molecular layer of the
777 primate dorsal cochlear nucleus. Neuroscience 154(1):99-113.
778 Ryugo DK, Haenggeli CA, Doucet JR. 2003. Multimodal inputs to the granule cell domain of the
779 cochlear nucleus. Exp Brain Res 153(4):477-485.
780 Ryugo DK, Willard FH. 1985. The dorsal cochlear nucleus of the mouse: a light microscopic
781 analysis of neurons that project to the inferior colliculus. J Comp Neurol 242(3):381-396.
782 Saint Marie RL. 1996. Glutamatergic connections of the auditory midbrain: selective uptake and
783 axonal transport of D-[3H]aspartate. J Comp Neurol 373(2):255-270.
784 Saldana E, Feliciano M, Mugnaini E. 1996. Distribution of descending projections from primary
785 auditory neocortex to inferior colliculus mimics the topography of intracollicular
786 projections. J Comp Neurol 371(1):15-40.
787 Saldana E, Merchan MA. 1992. Intrinsic and commissural connections of the rat inferior
788 colliculus. J Comp Neurol 319(3):417-437.
789 Sanes DH, Geary WA, Wooten GF, Rubel EW. 1987. Quantitative distribution of the glycine
790 receptor in the auditory brain stem of the gerbil. J Neurosci 7(11):3793-3802.

Schofield BR. 2001. Origins of projections from the inferior colliculus to the cochlear nucleus in guinea pigs. J Comp Neurol 429(2):206-220.

Schofield BR. 2002. Ascending and descending projections from the superior olivary complex in guinea pigs: different cells project to the cochlear nucleus and the inferior colliculus. J Comp Neurol 453(3):217-225.

Schofield BR. 2010. Projections from auditory cortex to midbrain cholinergic neurons that project to the inferior colliculus. Neuroscience 166(1):231-240.

Shore SE, Vass Z, Wys NL, Altschuler RA. 2000. Trigeminal ganglion innervates the auditory brainstem. J Comp Neurol 419(3):271-285.

Spangler KM, Cant NB, Henkel CK, Farley GR, Warr WB. 1987. Descending projections from the superior olivary complex to the cochlear nucleus of the cat. J Comp Neurol 259(3):452-465.

Tamamaki N, Yanagawa Y, Tomioka R, Miyazaki J, Obata K, Kaneko T. 2003. Green fluorescent protein expression and colocalization with calretinin, parvalbumin, and somatostatin in the GAD67-GFP knock-in mouse. J Comp Neurol 467(1):60-79.

Tang J, Yang W, Suga N. 2012. Modulation of thalamic auditory neurons by the primary auditory cortex. J Neurophysiol 108(3):935-942.

Thompson AM. 2006. Inferior colliculus projections to pontine nuclei in guinea pig. Brain Res 1100(1):104-109.

Tisdale AD, Nakajima Y. 1976. Fine structure of synaptic vesicles in two types of nerve terminals in crayfish stretch receptor organs: influence of fixation methods. J Comp Neurol 165(3):369-386.

Uchizono K. 1965. Characteristics of excitatory and inhibitory synapses in the central nervous system of the cat. Nature 207(997):642-643.

Vater M, Habbicht H, Kossl M, Grothe B. 1992a. The functional role of GABA and glycine in monaural and binaural processing in the inferior colliculus of horseshoe bats. J Comp Physiol A 171(4):541-553.

Vater M, Kossl M, Horn AK. 1992b. GAD- and GABA-immunoreactivity in the ascending auditory pathway of horseshoe and mustached bats. J Comp Neurol 325(2):183-206.

Weedman DL, Ryugo DK. 1996a. Pyramidal cells in primary auditory cortex project to cochlear nucleus in rat. Brain Res 706(1):97-102.

Weedman DL, Ryugo DK. 1996b. Projections from auditory cortex to the cochlear nucleus in rats: synapses on granule cell dendrites. J Comp Neurol 371(2):311-324.

Willard FH, Ryugo DK. 1983. Anatomy of the central auditory system. In: Willott JF, editor. The Auditory Psychobiology of the Mouse. Springfield, IL: Charles C Thomas. p 201-304.

Winer JA, Diehl JJ, Larue DT. 2001. Projections of auditory cortex to the medial geniculate body of the cat. J Comp Neurol 430(1):27-55.

Winer JA, Larue DT, Pollak GD. 1995. GABA and glycine in the central auditory system of the mustache bat: structural substrates for inhibitory neuronal organization. J Comp Neurol 355(3):317-353.

Winer JA, Saint Marie RL, Larue DT, Oliver DL. 1996. GABAergic feedforward projections from the inferior colliculus to the medial geniculate body. Proc Natl Acad Sci U S A 93(15):8005-8010.

Winer JA, Schreiner CE, editors. 2011. The Auditory Cortex. New York: Springer.

836 Wright DD, Ryugo DK. 1996. Mossy fiber projections from the cuneate nucleus to the cochlear
837 nucleus in the rat. J Comp Neurol 365(1):159-172.
838 Yan J, Ehret G. 2002. Corticofugal modulation of midbrain sound processing in the house
839 mouse. Eur J Neurosci 16(1):119-128.
840 Yan J, Zhang Y, Ehret G. 2005. Corticofugal shaping of frequency tuning curves in the central
841 nucleus of the inferior colliculus of mice. J Neurophysiol 93(1):71-83.
842 Young ED, Spirou GA, Rice JJ, Voigt HF. 1992. Neural organization and responses to complex
843 stimuli in the dorsal cochlear nucleus. Philos Trans R Soc Lond B Biol Sci
844 336(1278):407-413.
845 Zeilhofer HU, Studler B, Arabadzisz D, Schweizer C, Ahmadi S, Layh B, Bosl MR, Fritschy JM.
846 2005. Glycinergic neurons expressing enhanced green fluorescent protein in bacterial
847 artificial chromosome transgenic mice. J Comp Neurol 482(2):123-141.
848 Zhan X, Pongstaporn T, Ryugo DK. 2006. Projections of the second cervical dorsal root
849 ganglion to the cochlear nucleus in rats. J Comp Neurol 496(3):335-348.
850 Zhan X, Ryugo DK. 2007. Projections of the lateral reticular nucleus to the cochlear nucleus in
851 rats. J Comp Neurol 504(5):583-598.
852 Zhou X, Jen PH. 2005. Corticofugal modulation of directional sensitivity in the midbrain of the
853 big brown bat, Eptesicus fuscus. Hear Res 203(1-2):201-215.
854

Figure Legends

Figure 1. Photomicrographs of the IC in a GAD67-EGFP transgenic mouse following CTB injections into the DCN. **(A)** Multiunit frequency tuning curve at the DCN injection site with best frequency of 28 kHz. **(B)** Injection site in the DCN. Scale bar = 250 µm. **(C)** Coronal section of the IC from the same animal as in B. GABAergic cells are tagged with EGFP and shown in green. The narrow strip of labeled cells in the dorsolateral IC represent the GABA modules of ECIC2. Scale bar = 500 µm. **(D)** Higher-magnification of the ipsilateral IC in C. CTB-labeled cells are shown in magenta and do not co-localize with GABAergic neurons. Scale bar = 100 µm. **(E-F)** Higher-magnification of CTB-labeled cells shown in D. Scale bar = 25 µm. **(G)** Higher-magnification of the contralateral IC shown in C. Scale bar = 100 µm. **(H-I)** CTB-labeled cells in the contralateral IC also do not co-localize with EGFP. Scale bar = 25 µm.

Figure 2. Photomicrographs of the IC in a GAD67-EGFP transgenic mouse following FG injections into the DCN. **(A)** Multiunit frequency tuning curve at the DCN injection site with best frequency of 22 kHz. **(B)** Injection site in the DCN. Scale bar = 250 µm. **(C)** Coronal section of the IC from the same animal as in B. GABAergic cells are tagged with EGFP and shown in green. GABA modules are evident as narrow clusters of cells in the lateral part of the nucleus. Scale bar = 500 µm. **(D)** Higher-magnification of the ipsilateral IC in C. FG-labeled cells are shown in magenta and do not co-localize with GABAergic neurons. Scale bar = 100 µm. **(E-F)** Higher-magnification of FG-labeled cells shown in D. Scale bar = 25 µm. **(G)** Higher-magnification of the contralateral IC shown in C. Scale bar = 100 µm. **(H-I)** FG-labeled cells in the contralateral IC also do not co-localize with EGFP. Scale bar = 25 µm.

878 **Figure 3.** Photomicrographs of FG injection sites in the DCN and retrogradely labeled cells in
879 the IC of GAD67-EGFP transgenic mice. Each row displays an injection at a different
880 frequency region (A-E), along with high magnification images of the ipsilateral (F-J) and
881 contralateral (K-O) ICs illustrating that EGFP-positive GABAergic neurons (green) and FG-
882 labeled cells (magenta) do not co-label. These results demonstrate that descending IC
883 projections do not arise from GABAergic neurons. Scale bar in E = 250 μm and applies to
884 panels A-E. Scale bar in O = 25 μm and applies to panels F-O.
885 **Figure 4.** Analysis of counts, best frequency, and distribution of cells in the IC that project to the
886 DCN. **(A)** A modest relationship was observed between the best frequency at the DCN
887 injection site and the number of retrogradely labeled cells in the IC. Three cases were
888 incomplete, and are indicated with open circles. Linear regression with complete cases only
889 (n=11) indicated by solid line. Linear regression with all cases (n=14) indicated by dashed
890 line. **(B)** A significant relationship was found between frequency and the ratio of cell
891 numbers between the ipsilateral and contralateral ICs. Plot format as in A. **(C)** No
892 relationship was observed between total cell counts and the ratio of cells between IC
893 hemispheres. Plot format as in A. **(D)** Distribution of cell numbers in the IC for all cases,
894 separated by hemisphere and by IC subdivision. Asterisks indicate cases with incomplete IC
895 recovery. Means given for all cases (*, n=14) or for complete cases only (n=11). **(E)**
896 Distribution of cell numbers as in D, normalized by total cell count for each case. Format as
897 in D. **(F)** Distribution of cell numbers within each IC subdivision, normalized by total cell
898 count for each hemisphere for each case. Format as in D. Individual cases are vertically
899 aligned across panels D-F and sorted by ascending best frequency.

Figure 5. Representative and symmetrical distribution of retrogradely labeled cells in the IC of three individual cases following injections into the DCN. **(A)** A subset of coronal sections from one case (also shown in panels D and G). Note the presence of cells in all subdivisions, as well as an ipsilateral bias. Dashed line in ECIC indicates border between the third layer (ECIC3) and outer layers (ECIC1/2). Abbreviations: CB, cerebellum; CNIC, central nucleus of the IC; DCIC, dorsal cortex of the IC; ECIC, external cortex of the IC; PAG, periaquaductal grey; SC, superior colliculus. Numbers indicate distance (in sections) from caudal edge. Section thickness = 50 µm. **(B-G)** Quantification of symmetrical distribution of cells from the ipsilateral (color; reflected over midline) and contralateral (black) hemispheres for three cases within the coronal (B-D) and horizontal (E-G) planes. Ipsi- and contralateral histograms were independently normalized in each panel in order to compare relative distributions. Solid lines/boxes indicate the central distribution (mean ± SD) of cells along each histogram axis. Histogram axes in the coronal plane were rotated 45° to approximate the tonotopic organization of the IC. Both histograms and central distribution-boxes highlight bilateral symmetry in the locations of retrogradely labeled cells, and also suggest tonotopic specificity. Bin width = 100 µm. Grey lines indicate borders of the contralateral IC of all sections. All cases are shown in the same normalized coordinate space.

Figure 6. Distribution of retrogradely labeled cells in the IC from all cases within the coronal (A) and horizontal (B) planes. Each IC was normalized (see methods) such that all cells were plotted in the same coordinate space. Ipsilateral cells (grey) greatly outnumber contralateral cells (black). The majority of cells reside centrally within the IC, however labeled cells could be found at the extremes of all three principal axes in both hemispheres.

923 Histogram axes in the coronal plane were rotated 45°. Bin width = 50 µm. Grey lines
924 indicate the average borders of the IC (see methods).

925 **Figure 7.** Distribution of glycinergic neurons in the brain stem of a CBGlyT2-EGFP mouse.
926 Glycinergic neurons express EGFP and are shown in green. **(A)** A coronal section of the IC
927 reveals no EGFP labeled neurons, and thus, no glycinergic somata. Approximate IC
928 boundary marked by dashed line. Scale bar = 250 µm. **(B)** High magnification image of
929 EGFP labeled fibers and terminals from A. Scale bar = 50 µm. **(C)** EGFP-labeled
930 glycinergic neurons in a coronal section showing the nuclei of the trapezoid body. Scale bar
931 = 250 µm. **(D)** Higher magnification of EGFP labeled neurons in the medial nucleus of the
932 trapezoid body from C. Scale bar = 100 µm.

933 **Figure 8.** Distribution of cholinergic neurons in the brain stem of a CBA/CaH mouse. Cholinergic
934 neurons are stained brown following immunoprocessing. **(A)** A coronal section of the IC
935 reveals no ChAT-stained somata. Approximate IC boundary marked by dashed line. Scale bar
936 = 250 µm. **(B)** High magnification image of ChAT-positive endings in the IC from A. Scale
937 bar = 50 µm. **(C)** ChAT-positive neurons in the ventral nucleus of the trapezoid body. Scale
938 bar = 250 µm. **(D)** Higher magnification image of ChAT-positive neurons in C. Scale bar =
939 100 µm.

940 **Figure 9.** Anterogradely-labeled terminals are observed bilaterally in the DCN after an injection of
941 BDA in the IC. **(A)** Multiunit frequency tuning curve at the IC injection site with a best
942 frequency of 27 kHz. **(B)** A coronal section of the IC showing the BDA/CTB injection site.
943 Note the homotopic terminal field in the contralateral IC. Scale bar = 250 µm. **(C)** BDA-
944 labeled fibers (black) in the ipsilateral DCN. The tissue was faintly counterstained for Nissl
945 substance (blue). **(D)** High magnification of labeled fibers and terminals from C. Dashed lines

indicate approximate limits of layer II. **(E)** BDA-labeled fibers in the contralateral DCN of the same section as C-D. **(F)** High magnification of labeled fibers and terminals (black) and CTB-labeled neurons (brown) from E. **(G-J)** Similar results from an additional section 120 µm anterior to that shown in C-F. The projection to each DCN is topographic with the ipsilateral terminal field appearing more diffuse than that of the contralateral side. Labeled boutons are most prominent in layers II and III and occasionally terminate in layer I (D and J). Scale bar in I = 100 µm and also applies to panels C, E, and G. Scale bar in J = 50 µm and also applies to panels D, F, and H.

Figure 10. Electron micrographs of BDA-labeled terminals in the DCN. Columns represent examples from three different animals with injections placed at different frequencies in the CNIC. Top row illustrates labeled endings in the DCN ipsilateral to the injection site (A-C); bottom row demonstrates contralateral terminals (D-F). Note the homogeneous appearance of labeled endings. Scale bar in F = 500 nm and applies to all panels.

Figure 11. Electron micrographs of asymmetric PSDs formed by BDA-labeled endings on their targets in the DCN. Columns represent examples from three different animals with injections placed at different frequencies in the CNIC. Top row illustrates synapses ipsilateral to the injection (A-C); bottom row includes examples of contralateral synapses (D-F). All collicular terminals in the DCN exhibited asymmetric PSDs (indicated between arrowheads). Scale bar in F = 500 nm and applies to all panels.

Figure 12. Co-labeling of axons originating from the ipsilateral IC with VGlut2-positive endings in the DCN. **(A)** Maximum intensity projection confocal image shows a pair of descending projections from the IC labeled with ME (green) terminating in layer III of the ipsilateral DCN. Prominent boutons are indicated by arrowheads (white). **(B)** Maximum intensity

969 projection confocal image showing VGlut2-positive puncta (magenta) in the same region
970 displayed in A. **(C)** Color-merge of panels A and B. Co-labeling of ME and VGlut2 appears
971 white. **(D)** Detail of bouton shown in C. White lines indicate positions of orthogonal cross-
972 sections. **(E-F)** Orthogonal cross-sections show co-labeling of the bouton from D is
973 constrained in all three dimensions. **(G-I)** Detail of co-labeling for bouton cluster in C,
974 following same convention as in D-F. Scale bar in C = 10 µm and applies to panels A-C.
975 Scale bar in I = 5 µm and applies to panels D-I.
976

TABLE 1. List of antibodies used

Name	Immunogen	Manufacturer	Concentration
Anti-CTB	Purified choleragenoid (CTB aggregate)	List Biological Laboratories, Goat Polyclonal, Cat #703, RRID:AB_10013220	1:10,000
Anti-ChAT	Recombinant protein corresponding to the C-terminal portion of the human ChAT molecule	Vector Laboratories, Mouse Monoclonal, Cat #VP-C383, RRID:AB_2336337	1:1,000
Anti-VGluT2	Synthetic peptide located near the C-terminus of rat VGluT2 (amino acids 520-538). The sequence is identical in mouse and human VGluT2 and has no homology to VGluT1.	Sigma-Aldrich, Rabbit Polyclonal, Cat# V-2514, RRID:AB_477611	1:1,000

Table 2. Injection details and counts of labeled cells in the inferior colliculus.

Mouse		DCN injection			IC cell counts											
					Ipsilateral					Contralateral					Both	Ratio
ID	Strain	Freq. (kHz)	Tracer	Survival (days)	CNIC	ECIC 3	ECIC 1/2	DCIC	Total	CNIC	ECIC 3	ECIC 1/2	DCIC	Total	Total	(ipsi/contra)
AM326*	CBA/CaH	8	CTB/ME	11	92	16	8	11	127	36	3	4	1	44	171*	2.89*
AM341**	CBA/CaH	27	CTB/ME	10	180	21	32	13	246	50	10	16	2	78	324**	3.15**
AM342**	CBA/CaH	16	CTB/ME	10	27	2	9	12	50	9	1	4	7	21	71**	2.38**
AM484	GAD67-EGFP	23	CTB	11	151	41	19	22	233	57	5	6	3	71	304	3.28
AM485	GAD67-EGFP	28	CTB	11	145	23	34	14	216	58	3	3	0	64	280	3.38
AM491	GAD67-EGFP	22	FG	17	250	35	21	48	354	162	7	7	9	185	539	1.91
AM492	GAD67-EGFP	22	FG	18	162	8	9	2	181	118	4	2	0	124	305	1.46
AM505	GAD67-EGFP	29	FG/MR	18	165	16	6	5	192	69	7	5	1	82	274	2.34
AM521	GAD67-EGFP	23	FG/MR	14	267	23	37	29	356	128	9	14	9	160	516	2.23
AM532	GAD67-EGFP	24	FG/MR	18	130	7	8	4	149	53	5	2	0	60	209	2.48
AM583	GAD67-EGFP	10	FG/MR	17	15	0	0	0	15	25	0	0	0	25	40	0.6
AM584	GAD67-EGFP	15	FG/MR	17	28	2	0	2	32	13	0	0	0	13	45	2.46
AM597	GAD67-EGFP	35	FG/MR	17	176	13	18	15	222	43	2	7	4	56	278	3.96
AM622	GAD67-EGFP	40	FG/MR	10	189	22	15	9	235	46	5	3	0	54	289	4.35

* 3 sections excluded from counts

** 4 sections excluded from counts

Abbreviations: CNIC, central nucleus of the IC; CTB, cholera toxin subunit B; DCIC, dorsal nucleus of the IC; DCN, dorsal cochlear nucleus; ECIC, external cortex of the IC; FG, fluoro-gold; IC, inferior colliculus; ME, mini-emerald; MR, mini-ruby.

TABLE 3. List of abbreviations

AC	auditory cortex
BDA	biotinylated dextran amine
CN	cochlear nucleus
CNIC	central nucleus of the inferior colliculus
CTB	cholera toxin subunit B
DAB	3,3'-diaminobenzidine
DCIC	dorsal cortex of the inferior colliculus
DCN	dorsal cochlear nucleus
ECIC	external cortex of the inferior colliculus
EGFP	enhanced green fluorescent protein
FG	fluoro-gold
GABA	γ-aminobutyric acid
GAD67	glutamic acid decarboxylase 67
GCD	granule cell domain
GlyT2	glycine transporter 2
IC	inferior colliculus
ME	mini-emerald
MGB	medial geniculate body
MR	mini-ruby
SOC	superior olivary complex
VGluT2	vesicular glutamate transporter 2

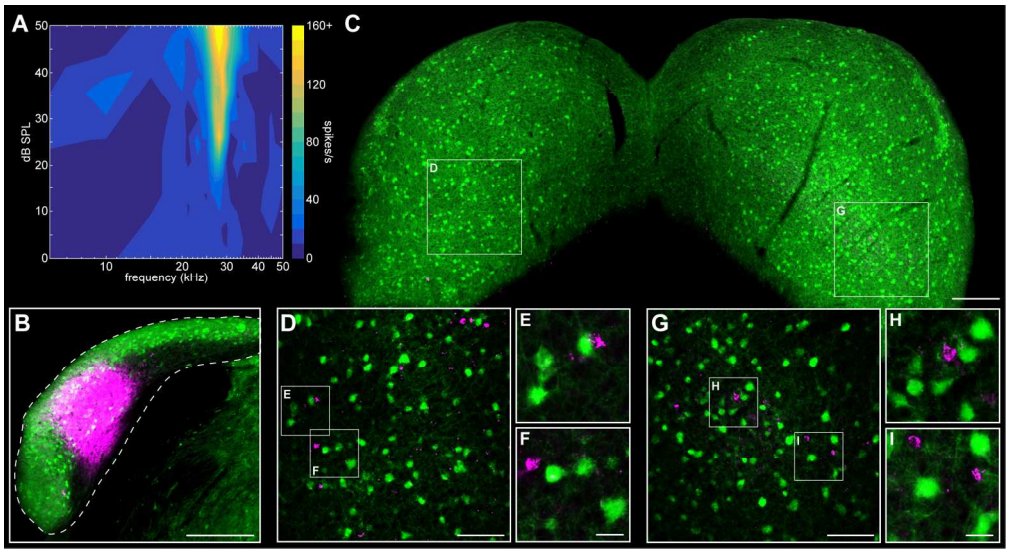

Photomicrographs of the IC in a GAD67-EGFP transgenic mouse following CTB injections into the DCN. **(A)** Multiunit frequency tuning curve at the DCN injection site with best frequency of 28 kHz. **(B)** Injection site in the DCN. Scale bar = 250 µm. **(C)** Coronal section of the IC from the same animal as in B. GABAergic cells are tagged with EGFP and shown in green. The narrow strip of labeled cells in the dorsolateral IC represent the GABA modules of ECIC2. Scale bar = 500 µm. **(D)** Higher-magnification of the ipsilateral IC in C. CTB-labeled cells are shown in magenta and do not co-localize with GABAergic neurons. Scale bar = 100 µm. **(E-F)** Higher-magnification of CTB-labeled cells shown in D. Scale bar = 25 µm. **(G)** Higher-magnification of the contralateral IC shown in C. Scale bar = 100 µm. **(H-I)** CTB-labeled cells in the contralateral IC also do not co-localize with EGFP. Scale bar = 25 µm.

Fig. 1

172x93mm (300 x 300 DPI)

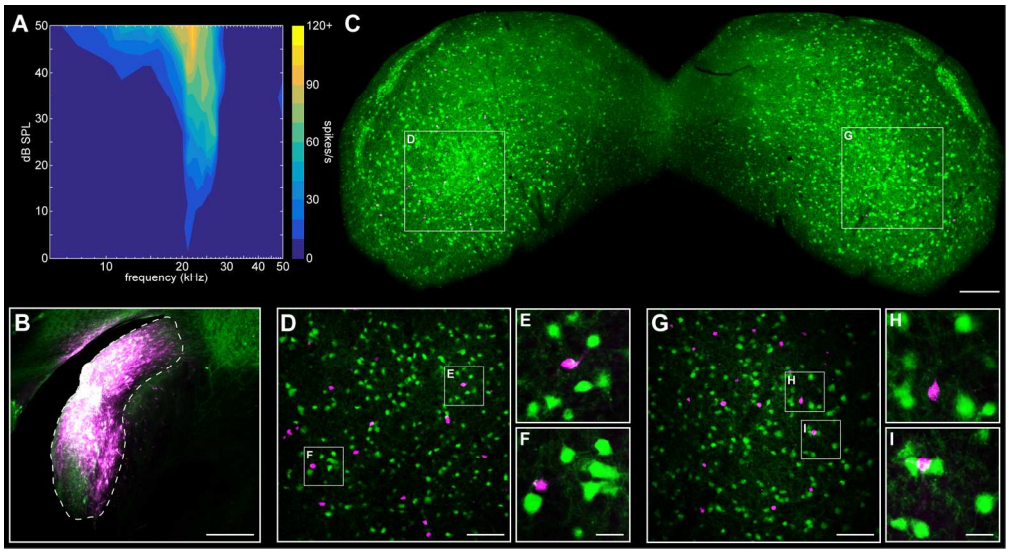

Photomicrographs of the IC in a GAD67-EGFP transgenic mouse following FG injections into the DCN. **(A)** Multiunit frequency tuning curve at the DCN injection site with best frequency of 22 kHz. **(B)** Injection site in the DCN. Scale bar = 250 µm. **(C)** Coronal section of the IC from the same animal as in B. GABAergic cells are tagged with EGFP and shown in green. GABA modules are evident as narrow clusters of cells in the lateral part of the nucleus. Scale bar = 500 µm. **(D)** Higher-magnification of the ipsilateral IC in C. FG-labeled cells are shown in magenta and do not co-localize with GABAergic neurons. Scale bar = 100 µm. **(E-F)** Higher-magnification of FG-labeled cells shown in D. Scale bar = 25 µm. **(G)** Higher-magnification of the contralateral IC shown in C. Scale bar = 100 µm. **(H-I)** FG-labeled cells in the contralateral IC also do not co-localize with EGFP. Scale bar = 25 µm.

Fig. 2

172x93mm (300 x 300 DPI)

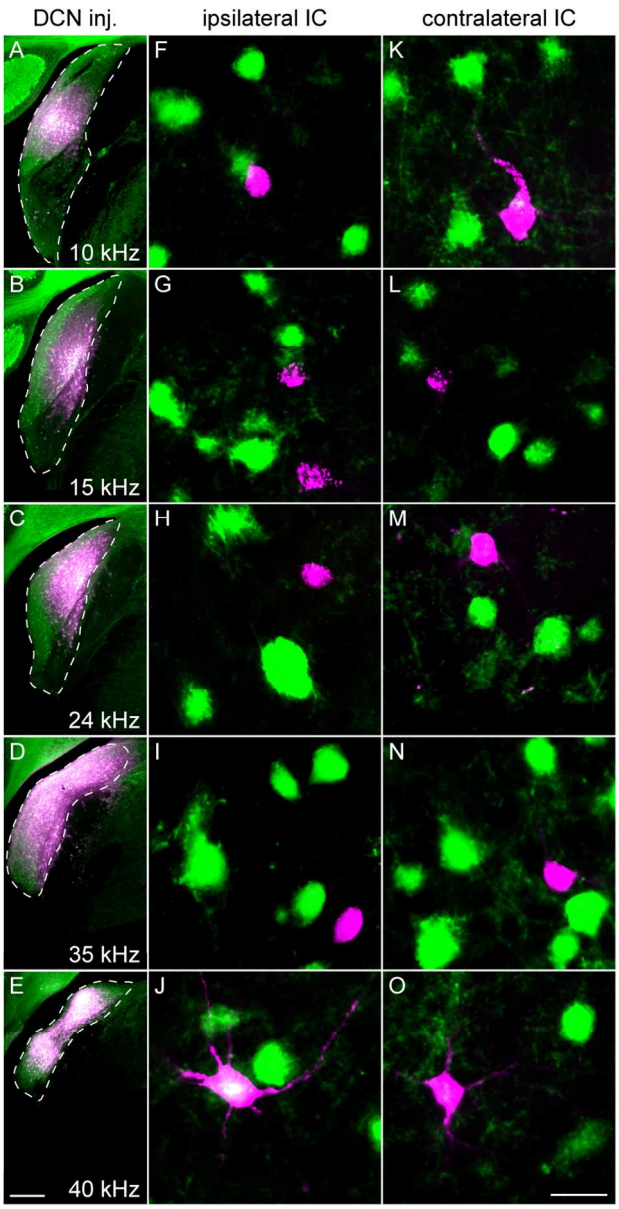

Photomicrographs of FG injection sites in the DCN and retrogradely labeled cells in the IC of GAD67-EGFP transgenic mice. Each row displays an injection at a different frequency region (A-E), along with high magnification images of the ipsilateral (F-J) and contralateral (K-O) ICs illustrating that EGFP-positive GABAergic neurons (green) and FG-labeled cells (magenta) do not co-label. These results demonstrate that descending IC projections do not arise from GABAergic neurons. Scale bar in E = 250 μm and applies to panels A-E. Scale bar in O = 25 μm and applies to panels F-O.

Fig. 3

81x158mm (300 x 300 DPI)

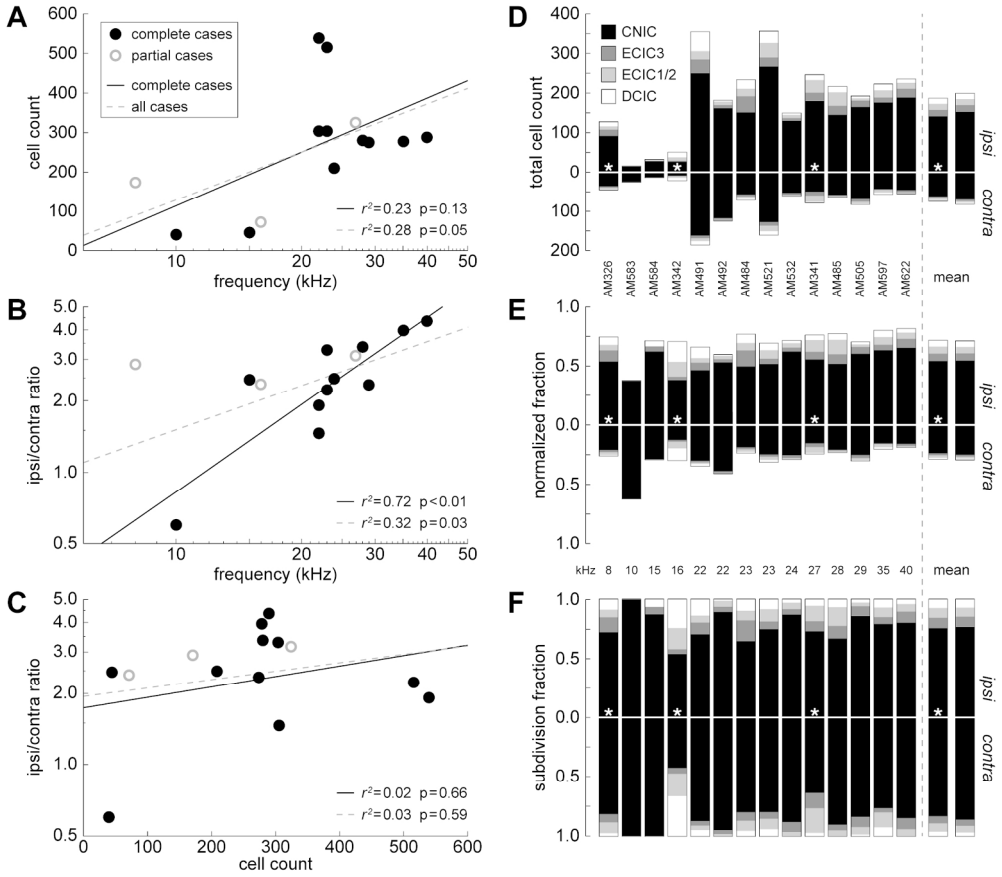

Analysis of counts, best frequency, and distribution of cells in the IC that project to the DCN. **(A)** A modest relationship was observed between the best frequency at the DCN injection site and the number of retrogradely labeled cells in the IC. Three cases were incomplete, and are indicated with open circles. Linear regression with complete cases only (n=11) indicated by solid line. Linear regression with all cases (n=14) indicated by dashed line. **(B)** A significant relationship was found between frequency and the ratio of cell numbers between the ipsilateral and contralateral ICs. Plot format as in A. **(C)** No relationship was observed between total cell counts and the ratio of cells between IC hemispheres. Plot format as in A. **(D)** Distribution of cell numbers in the IC for all cases, separated by hemisphere and by IC subdivision. Asterisks indicate cases with incomplete IC recovery. Means given for all cases (*, n=14) or for complete cases only (n=11). **(E)** Distribution of cell numbers as in D, normalized by total cell count for each case. Format as in D. **(F)** Distribution of cell numbers within each IC subdivision, normalized by total cell count for each hemisphere for each case. Format as in D. Individual cases are vertically aligned across panels D-F and sorted by ascending best frequency.

Fig. 4
172x150mm (300 x 300 DPI)

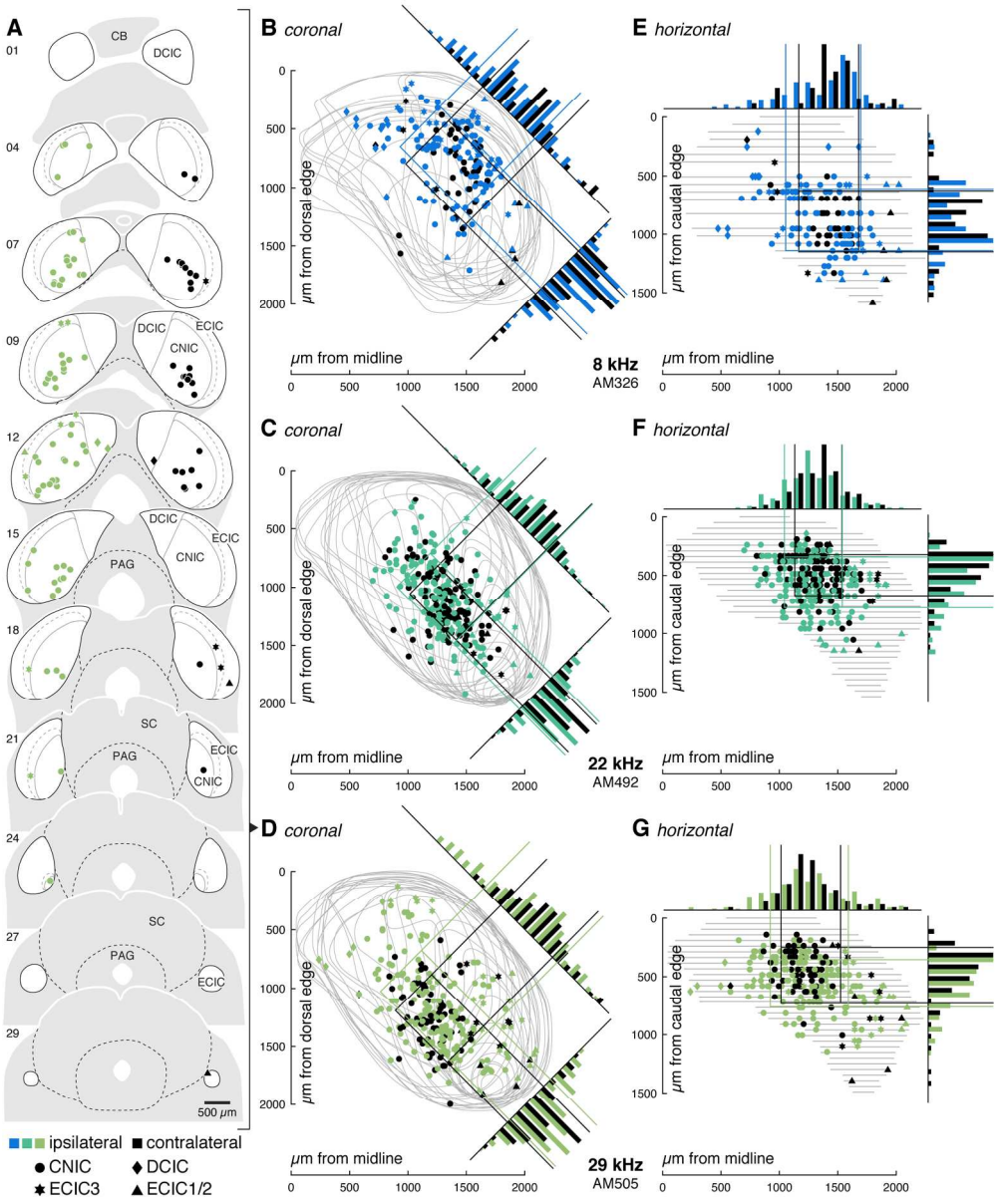

Representative and symmetrical distribution of retrogradely labeled cells in the IC of three individual cases following injections into the DCN. **(A)** A subset of coronal sections from one case (also shown in panels D and G). Note the presence of cells in all subdivisions, as well as an ipsilateral bias. Dashed line in ECIC indicates border between the third layer (ECIC3) and outer layers (ECIC1/2). Abbreviations: CB, cerebellum; CNIC, central nucleus of the IC; DCIC, dorsal cortex of the IC; ECIC, external cortex of the IC; PAG, periaquaductal grey; SC, superior colliculus. Numbers indicate distance (in sections) from caudal edge. Section thickness = 50 µm. **(B-G)** Quantification of symmetrical distribution of cells from the ipsilateral (color; reflected over midline) and contralateral (black) hemispheres for three cases within the coronal (B-D) and horizontal (E-G) planes. Ipsi- and contralateral histograms were independently normalized in each panel in order to compare relative distributions. Solid lines/boxes indicate the central distribution (mean ± SD) of cells along each histogram axis. Histogram axes in the coronal plane were rotated 45° to approximate the tonotopic organization of the IC. Both histograms and central distribution-boxes highlight bilateral symmetry in the locations of retrogradely labeled cells, and also suggest tonotopic

specificity. Bin width = 100 µm. Grey lines indicate borders of the contralateral IC of all sections. All cases are shown in the same normalized coordinate space.

Fig. 5

172x206mm (300 x 300 DPI)

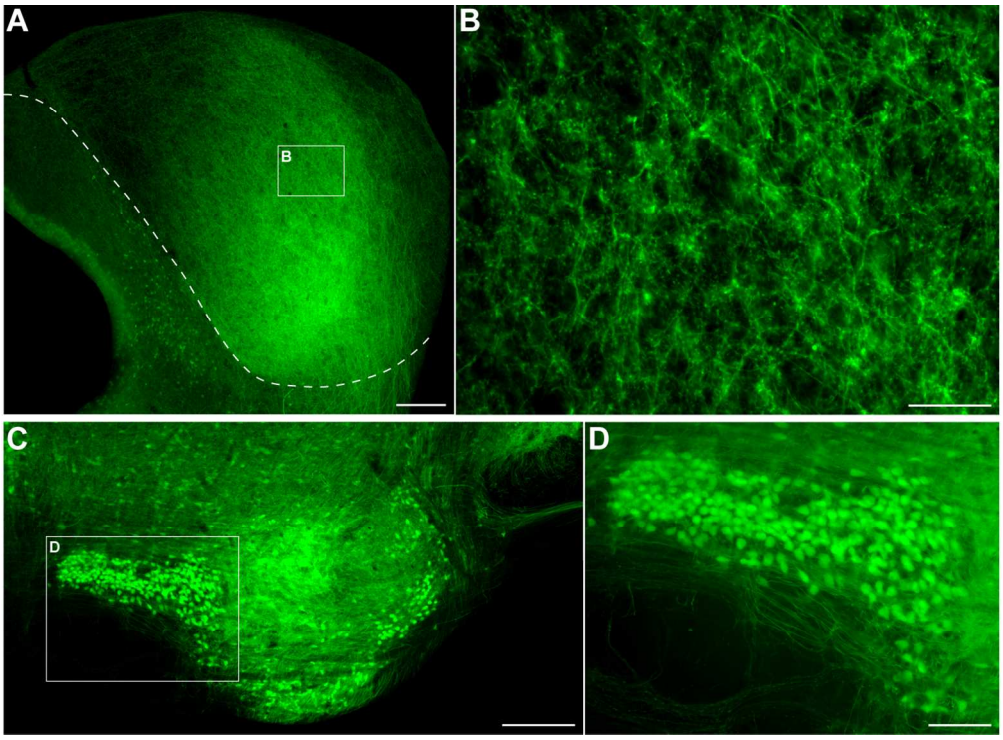

Distribution of glycinergic neurons in the brain stem of a CBGlyT2-EGFP mouse. Glycinergic neurons express EGFP and are shown in green. **(A)** A coronal section of the IC reveals no EGFP labeled neurons, and thus, no glycinergic somata. Approximate IC boundary marked by dashed line. Scale bar = 250 µm. **(B)** High magnification image of EGFP labeled fibers and terminals from A. Scale bar = 50 µm. **(C)** EGFP-labeled glycinergic neurons in a coronal section showing the nuclei of the trapezoid body. Scale bar = 250 µm. **(D)** Higher magnification of EGFP labeled neurons in the medial nucleus of the trapezoid body from C. Scale bar = 100 µm.

Fig. 7

130x94mm (300 x 300 DPI)

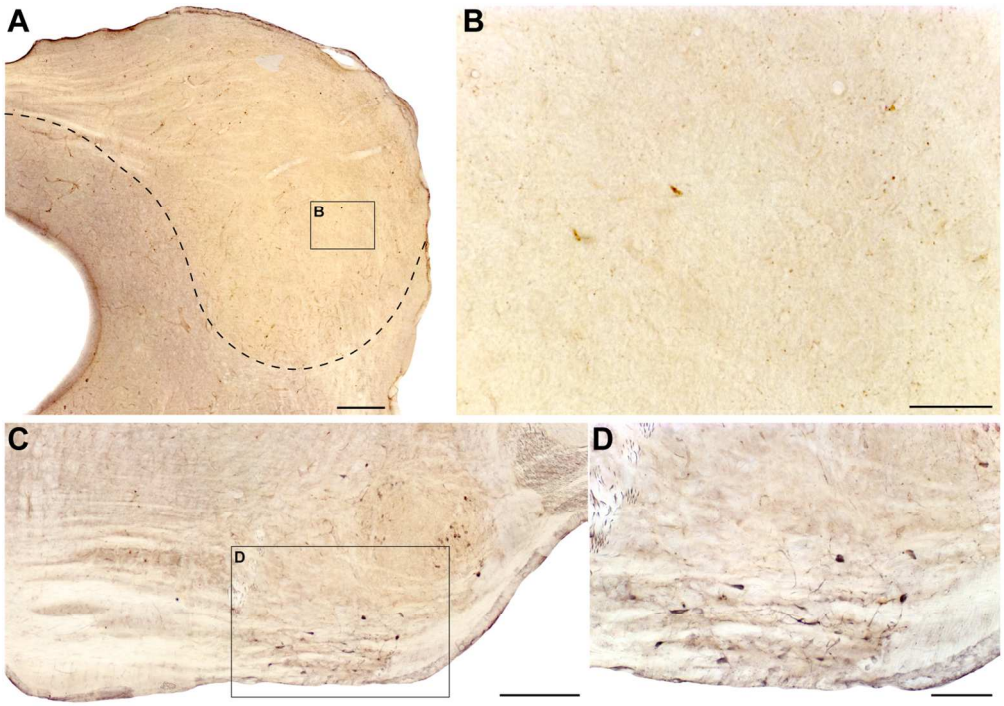

Distribution of cholinergic neurons in the brain stem of a CBA/CaH mouse. Cholinergic neurons are stained brown following immunoprocessing. **(A)** A coronal section of the IC reveals no ChAT-stained somata. Approximate IC boundary marked by dashed line. Scale bar = 250 µm. **(B)** High magnification image of ChAT-positive endings in the IC from A. Scale bar = 50 µm. **(C)** ChAT-positive neurons in the ventral nucleus of the trapezoid body. Scale bar = 250 µm. **(D)** Higher magnification image of ChAT-positive neurons in C. Scale bar = 100 µm.

Fig. 8

130x92mm (300 x 300 DPI)

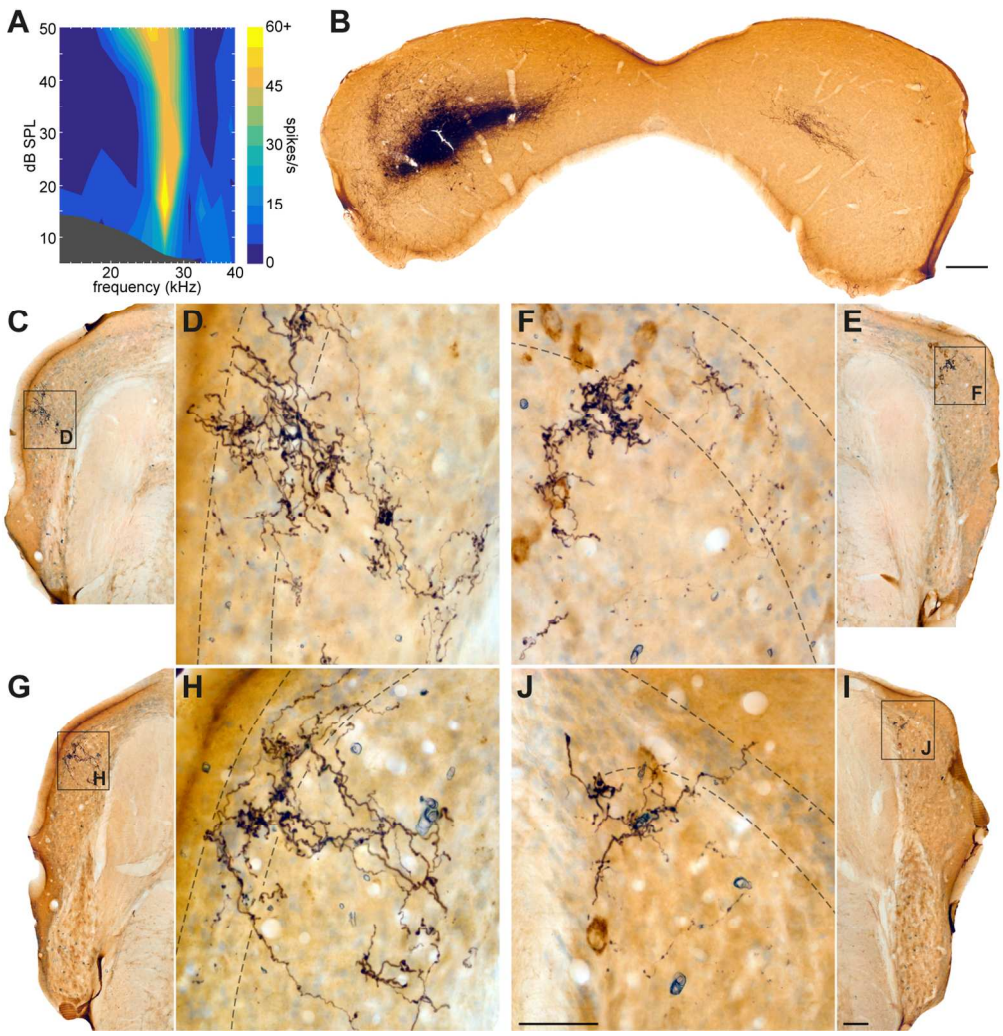

Anterogradely-labeled terminals are observed bilaterally in the DCN after an injection of BDA in the IC. **(A)** Multiunit frequency tuning curve at the IC injection site with a best frequency of 27 kHz. **(B)** A coronal section of the IC showing the BDA/CTB injection site. Note the homotopic terminal field in the contralateral IC. Scale bar = 250 µm. **(C)** BDA-labeled fibers (black) in the ipsilateral DCN. The tissue was faintly counterstained for Nissl substance (blue). **(D)** High magnification of labeled fibers and terminals from C. Dashed lines indicate approximate limits of layer II. **(E)** BDA-labeled fibers in the contralateral DCN of the same section as C-D. **(F)** High magnification of labeled fibers and terminals (black) and CTB-labeled neurons (brown) from E. **(G-J)** Similar results from an additional section 120 µm anterior to that shown in C-F. The projection to each DCN is topographic with the ipsilateral terminal field appearing more diffuse than that of the contralateral side. Labeled boutons are most prominent in layers II and III and occasionally terminate in layer I (D and J). Scale bar in I = 100 µm and also applies to panels C, E, and G. Scale bar in J = 50 µm and also applies to panels D, F, and H.

Fig. 9

130x133mm (300 x 300 DPI)

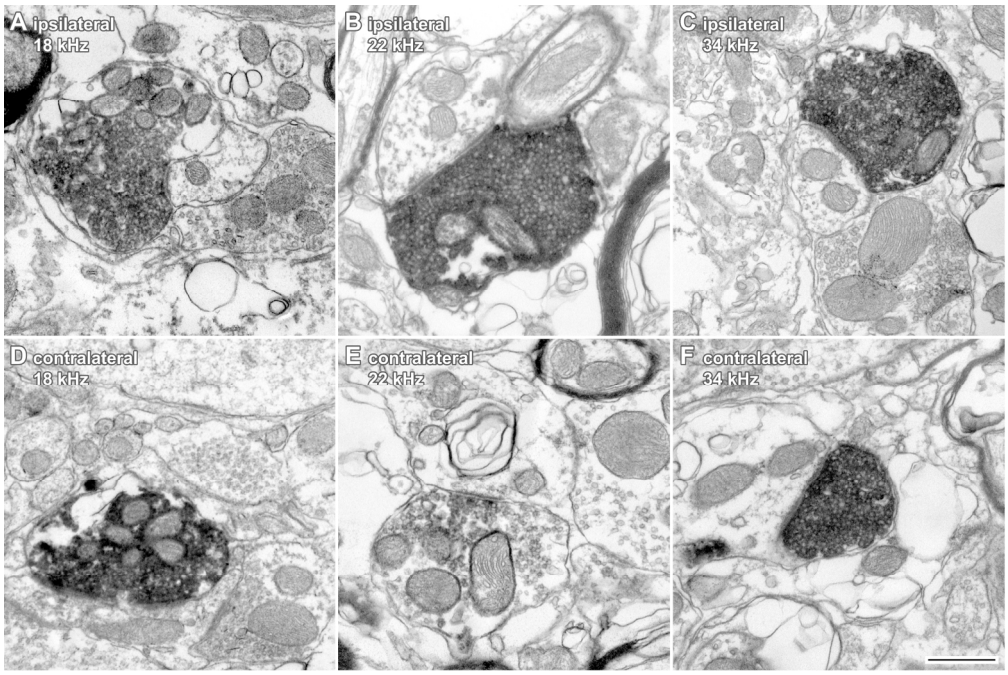

Electron micrographs of BDA-labeled terminals in the DCN. Columns represent examples from three different animals with injections placed at different frequencies in the CNIC. Top row illustrates labeled endings in the DCN ipsilateral to the injection site (A-C); bottom row demonstrates contralateral terminals (D-F). Note the homogeneous appearance of labeled endings. Scale bar in F = 500 nm and applies to all panels.
Fig. 10
172x114mm (300 x 300 DPI)

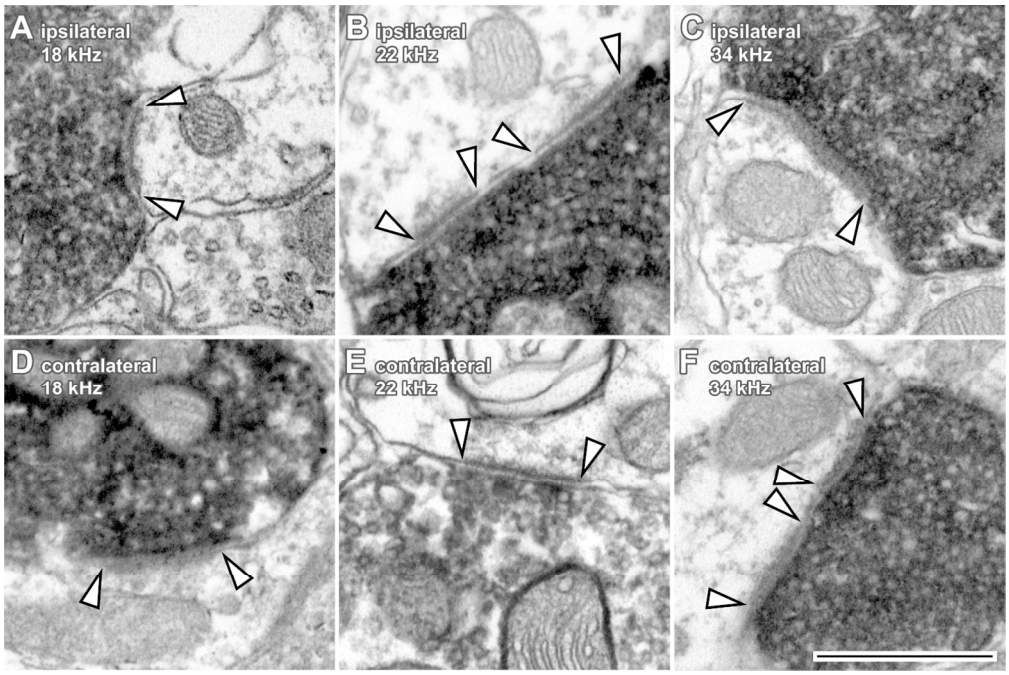

Electron micrographs of asymmetric PSDs formed by BDA-labeled endings on their targets in the DCN. Columns represent examples from three different animals with injections placed at different frequencies in the CNIC. Top row illustrates synapses ipsilateral to the injection (A-C); bottom row includes examples of contralateral synapses (D-F). All collicular terminals in the DCN exhibited asymmetric PSDs (indicated between arrowheads). Scale bar in F = 500 nm and applies to all panels.
Fig. 11
130x86mm (300 x 300 DPI)

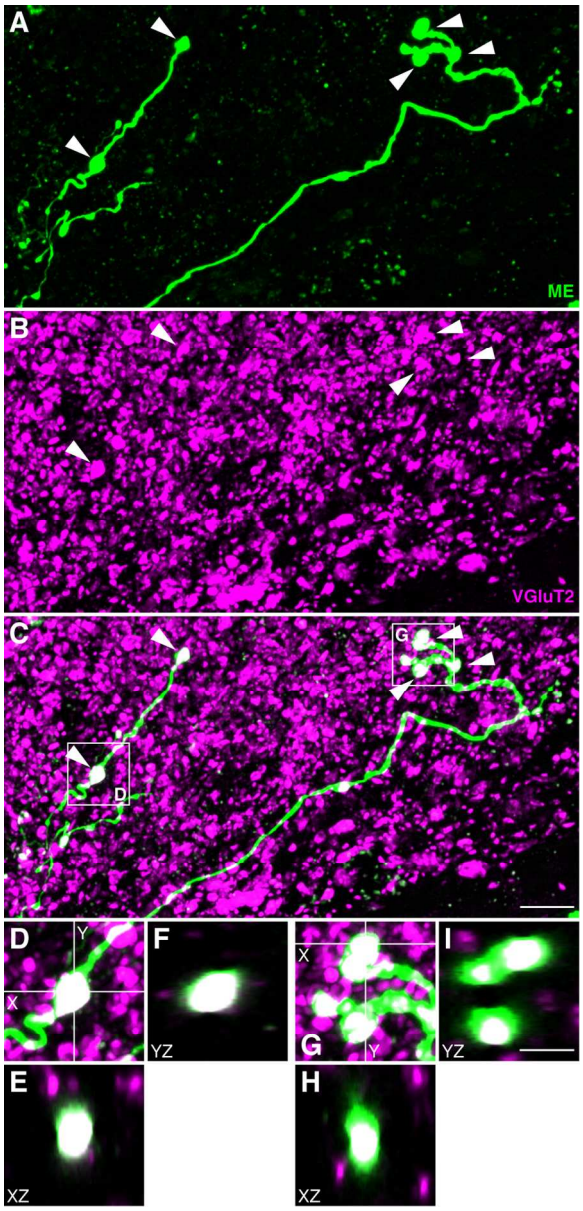

Co-labeling of axons originating from the ipsilateral IC with VGlut2-positive endings in the DCN. **(A)** Maximum intensity projection confocal image shows a pair of descending projections from the IC labeled with ME (green) terminating in layer III of the ipsilateral DCN. Prominent boutons are indicated by arrowheads (white). **(B)** Maximum intensity projection confocal image showing VGlut2-positive puncta (magenta) in the same region displayed in A. **(C)** Color-merge of panels A and B. Co-labeling of ME and VGlut2 appears white. **(D)** Detail of bouton shown in C. White lines indicate positions of orthogonal cross-sections. **(E-F)** Orthogonal cross-sections show co-labeling of the bouton from D is constrained in all three dimensions. **(G-I)** Detail of co-labeling for bouton cluster in C, following same convention as in D-F. Scale bar in C = 10 µm and applies to panels A-C. Scale bar in I = 5 µm and applies to panels D-I.

Fig. 12
81x169mm (300 x 300 DPI)

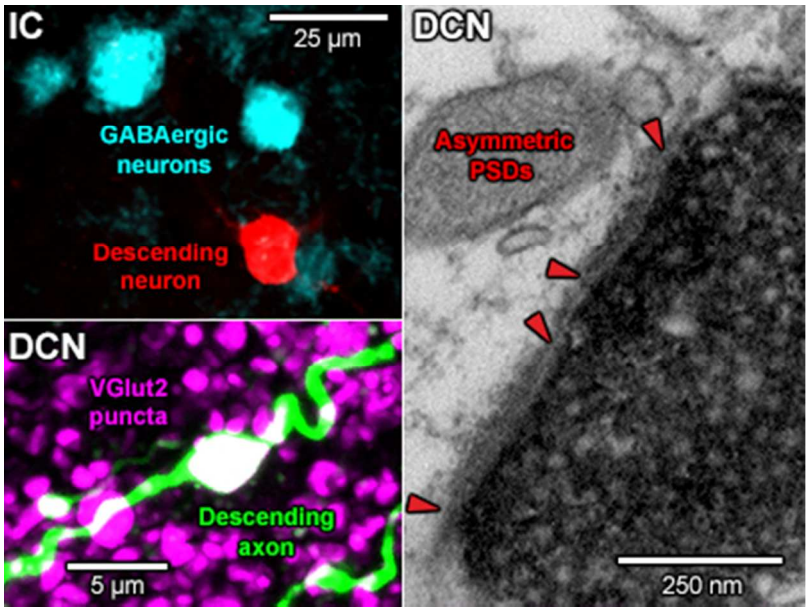

141x105mm (72 x 72 DPI)

Graphical Abstract:

We show the excitatory nature of bilateral descending projections from the inferior colliculus (IC) to the dorsal cochlear nucleus (DCN) via the absence of co-labeling with inhibitory IC neurons, along with the presence of axonal co-labeling with VGlut2-positive puncta and asymmetric postsynaptic densities in labeled terminals in the DCN.